RESEARCH ARTICLE

Check for updates

Using internal strain and mass to modulate Dy⋯Dy coupling and relaxation of magnetization in heterobimetallic metallofullerenes DyM₂N@C₈₀ and Dy₂MN@C₈₀ (M = Sc, Y, La, Lu)†

Yajuan Hao,[a,b] Georgios Velkos,[a] Sandra Schiemenz,[a] Marco Rosenkranz,[a] Yaofeng Wang,[a] Bernd Büchner,[a] Stanislav M. Avdoshenko, [ID] *[a] Alexey A. Popov [ID] *[a] and Fupin Liu [ID] *[a]

Endohedral clusters inside metallofullerenes experience considerable inner strain when the size of the hosting cage is comparably small. This strain can be tuned in mixed-metal metallofullerenes by combining metals of different sizes. Here we demonstrate that the internal strain and mass can be used as variables to control Dy⋯Dy coupling and relaxation of magnetization in Dy-metallofullerenes. Mixed-metal nitride clusterfullerenes $Dy_xY_{3-x}N@I_h$-C_{80} (x = 0–3) and $Dy_2LaN@I_h$-C_{80} combining Dy with diamagnetic rare-earth elements, Y and La, were synthesized and characterized by single-crystal X-ray diffraction, SQUID magnetometry, *ab initio* calculations, and spectroscopic techniques. $Dy_xY_{3-x}N$ clusters showed a planar structure, but the slightly larger size of Dy^{3+} in comparison with that of Y^{3+} resulted in increased elongation of the nitrogen thermal ellipsoid, showing enhancement of the out-of-plane vibrational amplitude. When Dy was combined with larger La, the Dy_2LaN cluster appeared strongly pyramidal with the distance between two nitrogen sites of 1.15(1) Å, whereas $DyLa_2N@C_{80}$ could not be obtained in a separable yield. Magnetic studies revealed that the relaxation of magnetization and blocking temperature of magnetization in the $DyM_2N@C_{80}$ series (M = Sc, Y, Lu) correlated with the mass of M, with $DySc_2N@C_{80}$ showing the fastest and $DyLu_2N@C_{80}$ the slowest relaxation. *Ab initio* calculations predicted very similar g-tensors for Dy^{3+} ground state pseudospin in all studied $DyM_2N@C_{80}$ molecules, suggesting that the variation in relaxation is caused by different vibrational spectra of these compounds. In the $Dy_2MN@C_{80}$ series (M = Sc, Y, La, Lu), the magnetic and hysteretic behavior was found to correlate with Dy⋯Dy coupling, which in turn appears to depend on the size of M^{3+}. Across the $Dy_2MN@C_{80}$ series, the energy difference between ferromagnetic and antiferromagnetic states changes from 5.6 cm^{-1} in $Dy_2ScN@C_{80}$ to 3.0 cm^{-1} in $Dy_2LuN@C_{80}$, 1.0 cm^{-1} in $Dy_2YN@C_{80}$, and −0.8 cm^{-1} in $Dy_2LaN@C_{80}$. The coupling of Dy ions suppresses the zero-field quantum tunnelling of magnetization but opens new relaxation channels, making the relaxation rate dependent on the coupling strengths. $DyY_2N@C_{80}$ and $Dy_2YN@C_{80}$ were found to be non-luminescent, while the luminescence reported for $DyY_2N@C_{80}$ was caused by traces of $Y_3N@C_{80}$ and $Y_2ScN@C_{80}$.

[a]*Leibniz Institute for Solid State and Materials Research (IFW Dresden), 01069 Dresden, Germany. E-mail: s.avdoshenko@ifw-dresden.de, a.popov@ifw-dresden.de, f.liu@ifw-dresden.de*

[b]*School of Electrical and Mechanical Engineering, Pingdingshan University, Pingdingshan 467000, China*

Introduction

Nitride clusterfullerenes with the molecular composition $M_3N@C_{2n}$ is one of the most versatile classes of endohedral metallofullerenes (EMFs).[1–6] The cage size ranges from C_{68} to C_{98} and even larger; however the highly symmetric I_h-C_{80} fullerene is usually most abundantly produced in the synthesis. The M_3N cluster has a triangular shape with a nitride ion in its center and three M(III) rare-earth metals located at the apexes of the triangle. Of particular interest is the possibility to combine two or even three different metals in the M_3N cluster in the arc-discharge process and the ability of chromato-

468 | *Inorg. Chem. Front.*, 2023, **10**, 468–484

This journal is © the Partner Organisations 2023

graphic techniques to separate mixtures of such heterometallic (mixed-metal) EMFs into individual components.[7–20] When specific interactions between metal ions are important, the mixed-metal approach provides the possibility to study such interactions by systematically varying the composition of the M_3N cluster. For instance, the magnetic properties of EMFs depend on the dipolar and exchange interactions between endohedral lanthanide ions,[21,22] and these interactions can be addressed by changing the number and type of magnetic ions in the heterobimetallic $M'_xM''_{3-x}N@C_{80}$ system (x = 0–3, M' and M'' are different rare-earth metals, including non-magnetic Sc, Y, La, or Lu, and magnetic 4f lanthanides).[22–31] Such a precise composition control in a virtually identical chemical environment is quite unique and rarely available for heterometallic systems in lanthanide chemistry.[32–38]

In this work, we employ the $M'_xM''_{3-x}N@C_{80}$ platform to study the influence of the internal strain on the static and dynamic magnetic properties of Dy-containing nitride clusterfullerenes. The use of external stimuli to modulate the properties of single molecule magnets has attracted significant attention as it opens the way for multifunctional magnetic systems.[39,40] Mechanical pressure was found to change both the ligand field and magnetic interactions in several transition-metal single-molecule magnets (SMMs),[41–48] but the studies of pressure-induced variations in the SMM behavior remain very scarce for lanthanide SMMs.[49–52] One of the main effects of mechanical pressure on molecular systems is the internal strain, which not necessarily requires the use of external pressure as it can be addressed by a judicious molecular design. Endohedral fullerenes provide an opportunity to engineer the internal strain through varying the size of the endohedral cluster. A fullerene cage is rather rigid and its size is usually not changed much when the internal species are varied. As a result, the endohedral M_3N cluster experiences a strain of different magnitude depending on the size of constituting metals.[53] This strain can be attested for via variation of different structural and physicochemical properties. For instance, the C_{80}-I_h fullerene cage is the most preferred for the metal-nitride cluster, and $M_3N@I_h$-C_{80} species are usually obtained with the highest yield among other cages, but when the metal ions are too large, the yield of EMFs decreases and the M_3N cluster changes its geometry from planar to pyramidal (M = Tb, Gd).[54,55] With a further increase of the metal size, the distribution shifts from C_{80} to larger cages, and for La and Ce, $M_3N@C_{80}$ is not formed at all.[56–58] Likewise, the preferable fullerene cage isomers can be changed depending on the size and shape of the endohedral cluster.[9,59–61] The size of the cluster and the associated internal strain were also shown to influence NMR and vibrational spectroscopic properties,[7,13,62] dynamics of the M_3N cluster inside the cage,[63,64] preferable cycloaddition sites,[65–68] and even electrochemical potentials of endohedral Ce(IV/III)[14,15] and Ti(IV/III)[69,70] redox couples. An earlier study demonstrated that the replacement of Sc by Lu in both $DySc_2N@C_{80}$ and $Dy_2ScN@C_{80}$ metallofullerenes resulted in the noticeable variation of their dynamic magnetic properties and Dy···Dy coupling.[24] The exact reasons why diamag-

netic metals can influence the magnetic behavior of Dy remained unclear as both the mass and size of the diamagnetic ion could play a certain role. Here we extend the $DyM_2N@C_{80}$ and $Dy_2MN@C_{80}$ series with further diamagnetic rare-earth metals, Y and La, and analyze the changes in internal strain and its relationship with magnetic properties when the size of the diamagnetic metal M is varied from Sc to La. Thanks to the different variations of the ionic radius and atomic mass in the Sc^{3+}–Y^{3+}–La^{3+}–Lu^{3+} series, we could distinguish two factors playing the main roles in the relaxation of magnetization of nitride clusterfullerenes, that is, the mass of M in the $DyM_2N@C_{80}$ series and the size-related strain in the $Dy_2MN@C_{80}$ series.

Synthesis and separation

Nitride clusterfullerenes were synthesized using a previously developed approach.[71] Dy–Sc and Dy–Lu nitride clusterfullerenes were obtained by us earlier,[13,24,71,72] and in this work the synthesis was performed for Dy–Y and Dy–La systems. A mixture of M_2O_3 (M = Y or La), Dy_2O_3, guanidinium thiocyanate and graphite powder with a molar ratio of 1 : 1 : 5 : 15 was filled in core-drilled graphite rods. The rods were evaporated by the direct current arc-discharge process in the chamber filled with He as a cooling gas (180 mbar). The produced soot was washed with acetone for 2 hours to remove the polyaromatic hydrocarbons, and then Soxhlet extracted with CS_2 overnight to dissolve the fullerenes. The CS_2 extract was separated by high-performance liquid chromatography (HPLC).

Fig. 1a and b show typical HPLC profiles of the extracts obtained in the Dy–Y and Dy–La EMF syntheses. The use of the organic nitrogen source suppresses the formation of empty fullerenes, and nitride clusterfullerenes become the main fullerene products.[73] The most abundant fraction in the Dy–Y system is the $Dy_xY_{3-x}N@I_h$-C_{80} mixture. According to mass-spectrometry analysis (Fig. 1c) and recycling HPLC (Fig. 1a), it contains components with all x from 0 to 3. This agrees with the similarity of the ionic radii of Dy^{3+} and Y^{3+}, which largely determines the probability of the EMF formation with a given cage size. The metals with substantially different ionic radii give a strong variation of the composition in the mixed-metal EMF synthesis,[13] and the Dy–La system is a good example of this behaviour. The overall yield of Dy–La EMFs is considerably lower than that of Dy–Y EMFs, and the main HPLC fraction is $Dy_3N@I_h$-C_{80} (Fig. 1b). $Dy_2LaN@C_{80}$ is found in the adjacent fraction with much lower abundance, whereas $DyLa_2N@C_{80}$ and $La_3N@C_{80}$ were not formed at all, at least in the amounts detectable by LDI-TOF MS. Apparently, the La^{3+} ion is too large, and the formation of $La_2MN@C_{80}$ was not detected even in the La–Sc system, with rather small Sc^{3+} ions.[74,75] As to La_3N-clusterfullerenes, the smallest cage able to accommodate the La_3N cluster is C_{88}.[57]

Individual target compounds were obtained by subjecting the respective fractions to recycling HPLC (Fig. 1a and b). The

This journal is © the Partner Organisations 2023

Inorg. Chem. Front., 2023, 10, 468–484 | 469

Fig. 1 (a) HPLC of the raw Dy–Y EMF extract, highlighting the main fraction (top) and recycling HPLC of this fraction giving individual compounds (bottom, the inset shows an enlarged 10th cycle). (b) HPLC of the raw Dy–La EMF extract, highlighting the fraction with the target compound (top) and recycling HPLC of this fraction giving individual $Dy_2LaN@C_{80}$ (bottom). (c) LDI mass spectra (positive ion mode) of a Y–Dy mixture and purified $DyY_2N@C_{80}$, $Dy_2YN@C_{80}$, and $Dy_2LaN@C_{80}$; insets show experimental and calculated isotopic patterns. Experimental conditions for linear HPLC: linear combination of two 10 × 250 mm Buckyprep columns; flow rate: 5 mL min^{-1}; injection volume: 4.5 mL; toluene as eluent; and 40 °C. Recycling HPLC: 10 × 250 mm Buckyprep (a) or Buckyprep-D (b) columns; flow rate: 1.0 mL min^{-1}; injection volume: 4.5 mL; and toluene as eluent.

$Dy_xY_{3-x}N@I_h$-C_{80} mixture is well resolved after 10 cycles, allowing collection of pure $Y_3N@I_h$-C_{80}, $DyY_2N@I_h$-C_{80}, and $Dy_2YN@I_h$-C_{80} in subsequent cycles, whereas $Dy_3N@I_h$-C_{80} still has an admixture of another isomer of $Y_3N@C_{80}$ with a D_{5h} cage, which has longer elution time than the I_h isomer. $Dy_2LaN@I_h$-C_{80} could be obtained after 4 cycles, the main admixtures being the tail of $Dy_3N@I_h$-C_{80} from the preceding fraction and sulphide clusterfullerene $Dy_2S@C_{82}$ formed due to the presence of sulfur in the nitrogen source.[76] The purity of isolated Dy–Y and Dy–La nitride clusterfullerenes was evaluated by laser desorption/ionization time-of-flight mass spectrometry (LDI-TOF MS) as shown in Fig. 1c. UV-vis-NIR and FT-IR absorption spectra of $DyY_2N@C_{80}$, $Dy_2YN@C_{80}$, and $Dy_2LaN@C_{80}$ (Fig. S1 and S2†) exhibit the characteristic pattern of $M_3N@I_h$-C_{80} EMFs.

Single-crystal X-ray diffraction

Molecular structures of $Dy_xY_{3-x}N@I_h$-C_{80} (x = 0–3) and $Dy_2LaN@I_h$-C_{80} were studied by single-crystal X-ray diffraction (SC-XRD). Crystals were obtained by co-crystallization of fullerenes with nickel(II) octaethylporphyrin (NiOEP). For this, benzene or CS_2 solutions of EMFs were layered with NiOEP solution in benzene in glass tubes and left to diffuse over 2–4 weeks, resulting in the formation of black block crystals on the walls. X-ray diffraction data collection was carried out at the BESSY storage ring (BL14.2, Berlin-Adlershof, Germany).[77] XDSAPP2.0 suite was employed for data processing.[78,79] The structure was solved by direct methods and refined using SHELXL-2018.[80] Hydrogen atoms were added geometrically

and refined with a riding model. The crystal data are presented in Tables S1 and S2.†

$Dy_xY_{3-x}N@I_h$-C_{80} (x = 0–3)

$M_3N@C_{80}$ molecules usually co-crystallize with NiOEP in one of the three space groups, $C2/c$ with 8 molecules, $C2/m$ with 4 molecules, and $P\bar{1}$ with 2 molecules in the unit cell (Table S3†). $C2/c$ is found in this work for $Y_3N@C_{80}$, $DyY_2N@C_{80}$, and $Dy_3N@C_{80}$. Their asymmetric unit contains one intact NiOEP molecule, one intact fullerene, one intact solvent benzene, and two halves of solvent benzene. $Dy_2YN@C_{80}$ crystallized in the $P\bar{1}$ space group, and its asymmetric unit contains one intact NiOEP molecule, one intact fullerene, and two intact solvent benzene molecules. The fullerene cage is ordered and unambiguously assigned to the $I_h(7)$ isomer in all four crystals, and the symmetry notation of $I_h(7)$-C_{80} will be omitted hereafter. The packing in the crystals, with one fullerene molecule supported by one NiOEP molecule, is also typical of EMF·NiOEP co-crystals.[72] An identical orientation of the fullerene cage *versus* NiOEP is found in all three crystals with the $C2/c$ space group, whereas the cage orientation of $Dy_2YN@C_{80}$ is somewhat different (Fig. 2).

Analysis of all reported $M_3N@I_h$-C_{80}·NiOEP crystal structures (see Table S3 in the ESI†) shows that unless the M_3N cluster is severely disordered, it usually has two M_3N sites, of which the major one has an occupancy of 0.7–0.9. The two sites share a common nitrogen position and are related by a rotation of 10–20° around an axis located nearly perpendicular to their M_3N planes so that the two sites appear roughly in one plane. This common pattern was found earlier for Gd_3N,[54] Dy_3N,[62] Ho_3N,[81] Er_3N,[81] Tm_3N,[82] Lu_3N,[64] $DyEr_2N$,[13] and

470 | *Inorg. Chem. Front.*, 2023, **10**, 468–484

This journal is © the Partner Organisations 2023

Fig. 2 Molecular structures in $M_3N@I_h$-C_{80}·NiOEP·$2C_6H_6$ single crystals: M_3N = Y_3N (a), DyY_2N (b), Dy_2YN (c), and Dy_3N (d). Top row: $M_3N@C_{80}$·NiOEP fragments; middle row: the structures of M_3N clusters with metal cite occupancies and bond lengths in Å for main sites; bottom row: different views of the M_3N clusters highlighting the shape of the nitrogen thermal ellipsoid. The displacement parameters are shown at the 30% probability, M−N bonds are shown as solid lines for the main site and as dotted lines for the site with the second highest occupancy. Color code: blue for nitrogen, cyan for yttrium, green for dysprosium sites with high occupancy and pale green for low-occupancy sites.

$DyGd_2N$,[13] and in this work for Y_3N, DyY_2N and Dy_3N (Fig. 2a, b and d). Dy_2YN shows a higher degree of disorder in the cluster (Fig. 2c).

The ionic radii of Y^{3+} (0.90 Å) and Dy^{3+} (0.91 Å) are rather similar, and it is therefore hard to expect that these metals will have different positions in $Y_2DyN@C_{80}$ and $YDy_2N@C_{80}$. The more plausible scenario is the uniform distribution of Y and Dy in all three positions in the M_3N cluster. Indeed, we could not differentiate between Dy and Y in the crystal structures of these fullerenes, and decided to apply free occupancy refinement on all possible metal positions with the relatively heavier Dy to identify the metal positions of DyY_2 and Dy_2Y. Since Y has fewer electrons than Dy, the maximal total occupancy of such "Dy^{3+}" sites should be 0.68 in DyY_2N and 0.84 in Dy_2YN. Despite the similarity of ionic radii, the influence of the metal size on the cluster is still discernible. With the stepwise replacement of Y^{3+} with Dy^{3+}, the shape of the nitrogen thermal ellipsoid gradually elongates in the direction perpendicular to the M_3 plane. This points to the increasing amplitude of the out-of-plane nitrogen vibration, which is associated with the trend towards M_3N pyramidalization with the increasing radius of M^{3+}. At the threshold between the planar and pyramidal clusters, the amplitude is the highest as shown in ref. 13, and this is the reason for a particular strong ellipsoid elonga-

tion found in Dy_3N here and also in an earlier report[62] (our new structure has different Dy_3N site occupancies but otherwise is very similar). We therefore refined the data with one position of N and the elongated ellipsoid, rather than splitting the nitrogen into two sites.

For $Y_3N@C_{80}$, a slightly pyramidal Y_3N cluster with a displacement of nitrogen from the Y_3 plane by 0.129(6) Å was reported in the pyrrolidine adduct,[83] while a planar Y_3N cluster was found in a phenyl-C_{81}-butyric acid methyl ester derivative.[84] In the co-crystal of pristine $Y_3N@C_{80}$ with NiOEP reported here for the first time, the Y_3N cluster is planar.

$Dy_2LaN@I_h$-C_{80}

$Dy_2LaN@C_{80}$ also co-crystallized with NiOEP in the $C2/c$ space group. The asymmetric unit contains one intact NiOEP molecule, one intact fullerene with two overlapping orientations, one intact solvent benzene, and two halves of solvent benzene. The fullerene cage is disordered between two orientations (site occupancy ratio of 0.61 : 0.39) as shown in Fig. 4a and S3,† which are correlated with a mirror plane passing through N–Ni–N bonds and perpendicular to the NiOEP molecule.

The Dy_2LaN cluster has considerable disorder with four metal sites (Fig. 4b), which hampers the reliable differentiation between Dy and La. We applied free occupancy refine-

This journal is © the Partner Organisations 2023

Inorg. Chem. Front., 2023, **10**, 468–484 | **471**

ment with the heavier Dy to identify the metal positions of Dy_2La. Note that for La uniformly distributed between three sites, the site occupancy of such "Dy" should be 0.94. The Dy_2LaN cluster is pyramidal and has two nitrogen sites (N1A/N1B with occupancies of 0.70/0.30), which is common for the M_3N cluster in $M_3N@C_{80}$ molecules with large metals, such as $DyGd_2N$,[13] $CeLu_2N$,[85] Tb_3N,[55] or Gd_3N.[54] The Dy_2LaN cluster has the highest sum of ionic radii of three M^{3+} ions among all $M_3N@C_{80}$ molecules studied by SC-XRD and shows the highest pyramidalization with an N1A/N1B out of M_3-plane displacement of 0.619(4)/0.530(9) Å determined for Dy1A/Dy2A/Dy3A sites with the largest occupancy, and an N1A⋯N1B distance of 1.15(1) Å. This can be compared to 0.522(8)/0.46(2) Å in Gd_3N (N⋯N distance: 0.991 Å),[54] 0.46(2)/0.45(2) Å in $DyGd_2N$ (0.91(3) Å),[13] 0.453(4)/0.405(7) Å in Tb_3N (0.858(8) Å),[55] and 0.349(8)/0.325(8) Å in $CeLu_2N$ (0.685(9) Å).[85] The M–N1A distances in the most abundant sites of Dy_2LaN are 2.095(4) (Dy1A), 2.082(3) (Dy2A), and 2.118(5) Å (Dy3A). For comparison, DFT predicts the Dy–N and La–N bonds in $Dy_2LaN@C_{80}$ to be 2.072 Å and 2.156 Å long, and the lack of a clear differentiation between Dy–N and La–N bond lengths in the crystal structure indicates that La is equally distributed between all metal positions. The same conclusion can also be made based on the occupancies of metal sites in Fig. 4b.

NiOEP has a considerable influence on the position of metal atoms inside the fullerene. In a vast majority of $M_3N@C_{80}$·NiOEP co-crystals, two metal atoms of the M_3N cluster are located above the N–Ni–N bonds.[63,64,81,86,87] The recently reported $Tb_2@C_{80}(CF_3)$ co-crystallized with NiOEP also shows such a tendency.[88] This effect seems to have an electrostatic nature as endohedral metals tend to be located close to negatively charged nitrogens of the porphyrin,[87] and this alignment was observed in the absence of Ni, when the $LaSc_2N@C_{80}$ fullerene was co-crystallized with H_2OEP.[75] Fig. 3 and S4† show that this pattern is also realized in $Dy_xY_{3-x}N@I_h$-C_{80} ($x = 0$–3) and $Dy_2LaN@I_h$-C_{80}. Even when the metals are disordered, the sites with the highest occupancy are located above NiOEP nitrogens.

Fig. 3 Orientation of endohedral DyY_2N and Dy_2LaN clusters with respect to NiOEP as representative examples of $M_3N@C_{80}$·NiOEP single crystals. Fullerene cage, C_2H_5 groups of NiOEP, and the solvent molecules are omitted for clarity. The displacement parameters are shown at a 30% probability. Color code: grey for carbon, blue for nitrogen, white for hydrogen, red for nickel, and green for metals in M_3N clusters.

Magnetic properties

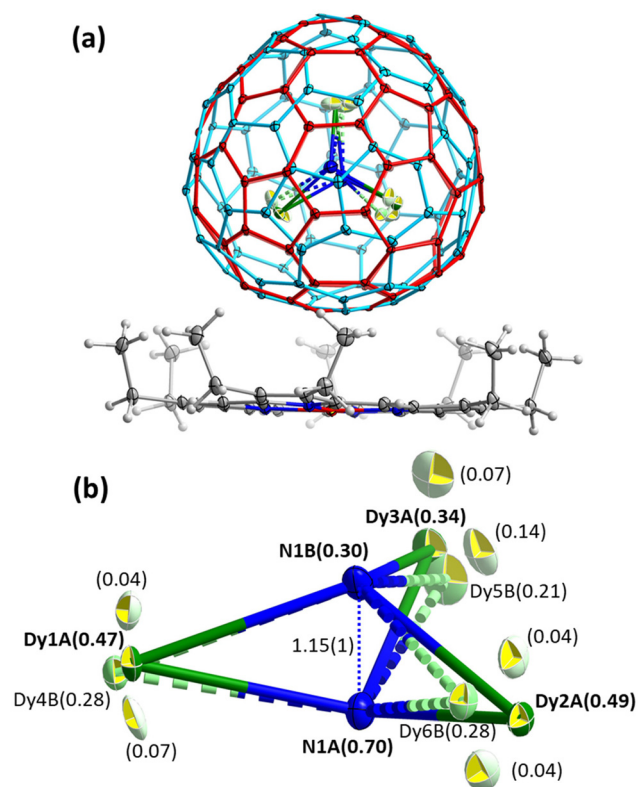### Structure of the M_3N cluster and single-ion magnetic anisotropy of Dy^{3+}

Confinement of the M_3N cluster inside the rigid fullerene cage results in a strain, which can be assessed through geometrical parameters of the cluster, such as the unusually short M–N bond lengths. For instance, the Dy–N bond length distribution in molecular compounds has a maximum near 2.5 Å, whereas Dy–N bonds in $M_3N@C_{80}$ are shorter than 2.1 Å (see Fig. 2 for examples from this work and ref. 13 for more details). This shortening has important consequences on magnetic properties since the negatively charged nitride ion (formal charge −3, Bader charge of $-1.7^{29,89}$) produces a strong uniaxial ligand field and hence leads to the large magnetic anisotropy of Dy^{3+}.

The structural parameters of the M_3N cluster can be further adjusted by the variation of its composition, and in particular by combining metals of different sizes. For instance, Y^{3+} is larger than Sc^{3+}, and the Dy–N bond in $DyY_2N@C_{80}$ (Fig. 2b) is shorter than that in $DySc_2N@C_{80}$ (2.096(6) Å according to SC-XRD[72]). Thus, combining Dy in M_3N with large metals might be considered as a strategy to shorten Dy–N bonds and thereby increase the magnetic anisotropy. However, this compression effect has its limits, and after a certain threshold, the M–N bonds will not be shortened anymore. Instead, the cluster changes its shape from planar to pyramidal with the nitride ion elevated above the metal plane.[13,54,55,81,85] Experimental examples for Dy-containing $M_3N@C_{80}$ characterized by SC-XRD are $DyGd_2N@C_{80}$ from ref. 13 and $Dy_2LaN@C_{80}$ described in this work (Fig. 4). As the ligand field is not purely an electrostatic phenomenon,[90] the influence of this geometrical change on the magnetic anisotropy is *a priori* not clear. To better understand it, we performed a systematic *ab initio* computational study for a series of $DyM_2N@C_{80}$ and $Dy_2MN@C_{80}$ molecules. A combination of Dy ($R^{3+} = 0.912$ Å) with Sc (0.745 Å), Lu (0.861 Å), Y (0.900 Å), Gd (0.938 Å), or La (1.032 Å) allows for a smooth variation of the cluster size. We used DFT-optimized structures from ref. 13 for this survey because not all SC-XRD structures are available, and the available ones often suffer from a significant degree of disorder, which prevents the analysis of a subtle variation of the M–N bond lengths (see Fig. 2 and 4). As the parameter describing the net size of metals in the M_3N cluster, the sum of their Shannon's ionic radii[91] ($\sum R^{3+}$) is used.

Fig. 5a illustrates the bond shortening and cluster pyramidalization trends in DFT-optimized structures. The Dy–N bond length ($d_{Dy–N}$) decreases fast with the increase of $\sum R^{3+}$ from 2.4 Å ($DySc_2N$) to 2.7 Å (DyY_2N), but then the shortening of $d_{Dy–N}$ stagnates and even reverses to a slight elongation in Dy_2LaN and $DyLa_2N$ when $\sum R^{3+}$ exceeds 2.8 Å. In parallel, the cluster pyramidalization (h_N) starts to grow when $\sum R^{3+}$ exceeds 2.7 Å, and the growth continues all the way up to $h_N = 0.82$ Å in the hypothetical $DyLa_2N@C_{80}$ with a $\sum R^{3+}$ of 2.98 Å.

Single-ion magnetic anisotropy of Dy^{3+} ions was then studied *ab initio* at the CASSCF(9,7)/RASSI-SO level in

472 | *Inorg. Chem. Front.*, 2023, **10**, 468–484

This journal is © the Partner Organisations 2023

Fig. 4 (a) Fragment of Dy$_2$LaN@I_h-C$_{80}$·NiOEP crystals showing fullerene and porphyrin; solvent molecules are omitted for clarity; two orientations of the fullerene cage are shown in red (0.61) and cyan (0.39). (b) The structure of the Dy$_2$LaN cluster in the crystal showing all metal and nitrogen sites (site occupancies are listed in parentheses). Selected bond lengths: N1A–Dy1A, 2.095(4) Å; N1A–Dy2A, 2.082(3) Å; N1A–Dy3A, 2.118(6) Å; N1B–Dy1A, 2.042(8) Å; N1B–Dy2A, 2.136(7) Å; and N1B–Dy3A, 2.05(1) Å. M–N bonds are shown as solid lines for the main metal site and as dotted lines for the site with the second highest occupancy.

OpenMOLCAS.[92,93] The Dy atoms in M$_3$N@C$_{80}$ molecules were treated one at a time, while other magnetic ions (Dy and Gd) were replaced with Y. The results of *ab initio* computations are summarized in Fig. 5b–d, and full data are given in Tables S4–S6.† The ground magnetic state of Dy^{3+} in all studied molecules is the Kramers doublet (KD) with essentially a pure m_J = ±15/2 character. For the rigorous m_J = ±15/2 KD, the principal values of the pseudospin g-tensor should be (0, 0, 20). In M$_3$N@C$_{80}$ molecules, g_z values are spread between 19.78 and 19.88 without any obvious regularity except for a vague trend to decrease for larger metals, and in particular for DyLa$_2$N@C$_{80}$ (Fig. 5b). The transversal components, quantified as $g_{x,y} = \sqrt{(g_x^2 + g_y^2)/2}$, exhibit a more regular variation with $\sum R^{3+}$. The $g_{x,y}$ value increases with the size of metals and closely follows h_N dependence. In fact, there is a good linear correlation between $g_{x,y}$ and h_N (Fig. S5†). Since the transversal components of the ground-state g-tensors define the tunnelling gap and thus determine the efficiency of the quantum tunnelling of magnetization (QTM) in zero magnetic field, the cluster pyramidalization may be considered an important

factor for the QTM. But in the DyM$_2$N@C$_{80}$ series, for which this kind of QTM is crucial, the strong cluster pyramidalization is achieved only in the experimentally non-available DyLa$_2$N@C$_{80}$, whereas in DyM$_2$N@C$_{80}$ with Sc, Lu, and Y the cluster is nearly planar.

Fig. 5c compares the size of the ligand-field splitting in the studied molecules focusing on the energy of the first excited KD (KD2) and on the whole splitting of the ground-state ^{6}H$_{15/2}$ multiplet (which is equal to the energy of the eighth KD, KD8). Selected examples of the LF splitting in individual DyM$_2$N@C$_{80}$ and Dy$_2$MN@C$_{80}$ molecules are shown in Fig. 5d. Both the overall LF splitting and the KD2 energy increase with $\sum R^{3+}$, but in a different fashion. E(KD8) shows two distinct segments in its growth, which are related to the nature of the structural changes. While d_{Dy-N} decreases (that is, for $\sum R^{3+}$ < 2.7 Å), the growth of E(KD8) is relatively fast, but beyond the cluster pyramidalization threshold, the growth of E(KD8) is slowed down. In contrast, E(KD2) grows continuously in the whole $\sum R^{3+}$ range, which can be well described by a quadratic function (Fig. 5c).

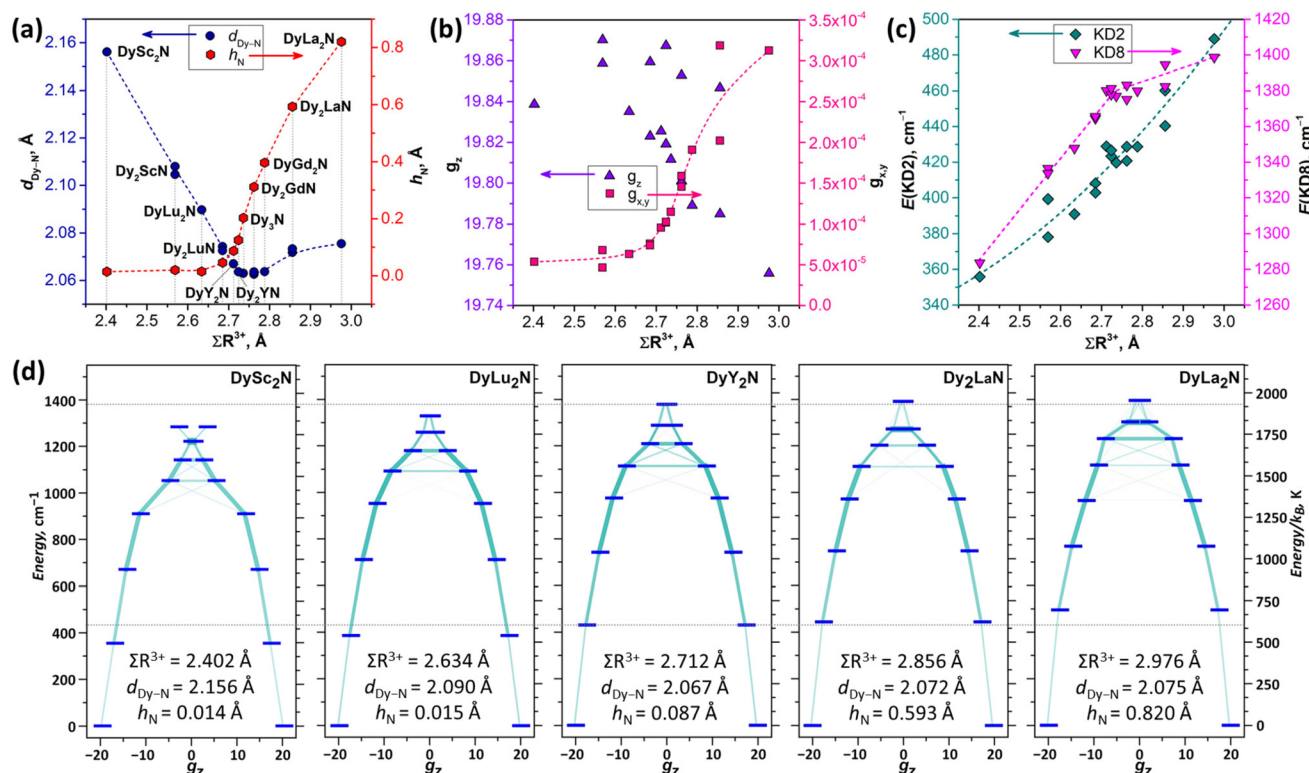To summarize, our computations showed that the ground magnetic state of Dy^{3+} in M$_3$N@C$_{80}$ molecules is weakly affected by the size of the metals forming the cluster and the variation of the cluster geometry. The transversal components of the g-tensors do increase with the cluster pyramidalization, but there is a lack of experimentally available molecules, where this effect may have a pronounced influence on magnetic behavior. Ligand field splitting is more susceptible to the cluster shape variations. The total splitting can be indeed related to the Dy–N bond length, and therefore it experiences only marginal changes when the metal size increase leads to cluster pyramidalization. But the energy of the first excited KD appears to be sensitive to the size-dependent strain itself, irrespective of the changes in the cluster geometry it causes.

Magnetic hysteresis

We next turn to the experimental studies of the magnetic properties of DyY$_2$N@C$_{80}$, Dy$_2$YN@C$_{80}$, and Dy$_2$LaN@C$_{80}$ by SQUID magnetometry. DyY$_2$N@C$_{80}$ shows waist-restricted (butterfly) magnetic hysteresis with an abrupt drop of magnetization near zero field (Fig. 6a). This feature is caused by the quantum tunnelling of magnetization (QTM) and is typical of single-ion Dy SMMs.[27,30,94–98] The hysteresis remains open up to 8 K when measured at a sweep rate of 2.9 mT s^{-1}. Determination of the blocking temperature T_B from the zero-field cooled/in-field cooled (ZFC/FC) temperature dependence of magnetic susceptibility gives a value of 8.4 K (Fig. 6a). Similar characteristics of magnetic hysteresis were obtained for DyY$_2$N@C$_{80}$ in a recent report by Wang *et al.*[30]

Magnetic hysteresis of Dy$_2$YN@C$_{80}$ remains open up to 5 K. Likewise, the hysteresis without distinct QTM features is measured for Dy$_2$LaN@C$_{80}$ up to 4 K (Fig. 7a). T_B values in Dy$_2$YN@C$_{80}$ and Dy$_2$LaN@C$_{80}$ are 4.7 and 3.3 K, respectively. The zero-field QTM feature in the hysteresis curves of both EMFs is absent, as is common for dinuclear EMF-SMMs.[22,24,99–101] The coupling of two magnetic moments

This journal is © the Partner Organisations 2023

Inorg. Chem. Front., 2023, **10**, 468–484 | **473**

Fig. 5 (a) Dy–N bond lengths (d_{Dy-N}) and M_3N pyramid height (elevation of N above the plane of metal atoms, h_N) in DFT-optimized $DyM_2N@C_{80}$ and $Dy_2MN@C_{80}$ molecules (M = Sc, Lu, Y, La, Gd) plotted *versus* the sum of Shannon's ionic radii of metals in the M_3N cluster ($\sum R^{3+}$). (b) Components of the pseudospin g-tensor, g_z and $g_{x,y}$ (root mean square of g_x and g_y) for the Dy^{3+} ground state Kramers doublet (KD1) in the same set of molecules. (c) The energy of the first excited KD (KD2) and the total ligand-field splitting (KD8) in the same set of molecules. Dashed lines in (a) and (b) are a spline interpolation added to guide the eye; in (c), the dashed line for E(KD2) is a quadratic fit. (d) Dy^{3+} ligand-field splitting with transition probabilities in selected $M_3N@C_{80}$ molecules along with their $\sum R^{3+}$, d_{Dy-N}, and h_N parameters; dotted lines are guides to the eye and mark the KD2 and KD8 energies in $DyY_2N@C_{80}$. Ligand-field splitting and pseudospin g-tensor parameters used in (b–d) are computed *ab initio* at the CASSCF/RASSI-SO level using DFT-optimized molecular structures.

prevents an independent QTM-flip of one of the moments in zero field,[22] whereas the simultaneous flip of both moments is a rare-probability process detectable only at very low temperatures.[102]

With the data from this work, we can compare hysteretic behaviour in complete sets of $DyM_2N@C_{80}$ and $Dy_2MN@C_{80}$ with the diamagnetic rare-earth M. Earlier we found that the T_B of $DyLu_2N@C_{80}$, 9.5 K, is higher than that of $DySc_2N@C_{80}$ by 2.6 K.[24] The value of 8.4 K determined here for $DyY_2N@C_{80}$ lies in between. Different from $DySc_2N@C_{80}$ and $DyY_2N@C_{80}$, $DyLu_2N@C_{80}$ showed some remanence and less efficient zero-field QTM.[24] Overall, the T_B in the $DyM_2N@C_{80}$ series increases from Sc to Y to Lu and thus tends to correlate with the increase of the atomic mass rather than the ionic radius in this row (Fig. 8a).

A different situation is found in the binuclear $Dy_2MN@C_{80}$ series. $Dy_2ScN@C_{80}$ and $Dy_2LuN@C_{80}$ showed similar T_B and hysteresis closing temperatures of 8 K, but with a narrower hysteresis in $Dy_2LuN@C_{80}$.[24] The new data from this work reveal a decrease of the blocking temperature on going from Dy_2LuN to Dy_2YN to Dy_2LaN (Fig. 8b), as well as a decrease of the 2 K coercive field in the Dy_2MN series, Sc (0.70 T) > Lu (0.44 T) > Y

(0.28 T) > La (0.09 T). The latter effect is illustrated in Fig. 7b, which compares the hysteresis curves of four EMFs. Thus, the hysteretic behaviour in the $Dy_2MN@C_{80}$ series changes systematically with the M^{3+} size.

Importantly, when the metal M in $DyM_2N@C_{80}$ or $Dy_2MN@C_{80}$ is paramagnetic, the hysteretic behaviour is quite different from those of its diamagnetic analogs. At 1.8 K, $Dy_3N@C_{80}$ shows only a narrow hysteresis with fast QTM in zero field, which is caused by the multiply degenerate frustrated ground state.[22] In $Dy_2GdN@C_{80}$, the presence of Gd accelerates the relaxation of magnetization when compared to $Dy_2ScN@C_{80}$ and $Dy_2YN@C_{80}$, so that only a very narrow hysteresis is open at 1.8 K.[23] In $DyGd_2N@C_{80}$, $DyEr_2N@C_{80}$, and $Dy_2ErN@C_{80}$, we could not find an open hysteresis down to 1.8 K (see Fig. S6† for magnetization curves; the synthesis is described in ref. 13).

Dy···Dy coupling in $Dy_2MN@C_{80}$

A considerable difference between the hysteresis curves of $DyY_2N@C_{80}$ and $Dy_2YN@C_{80}$ emphasizes that the interaction between the magnetic moments of Dy ions plays a crucial role in the static and dynamic magnetic behaviour, especially at

474 | *Inorg. Chem. Front.*, 2023, **10**, 468–484

This journal is © the Partner Organisations 2023
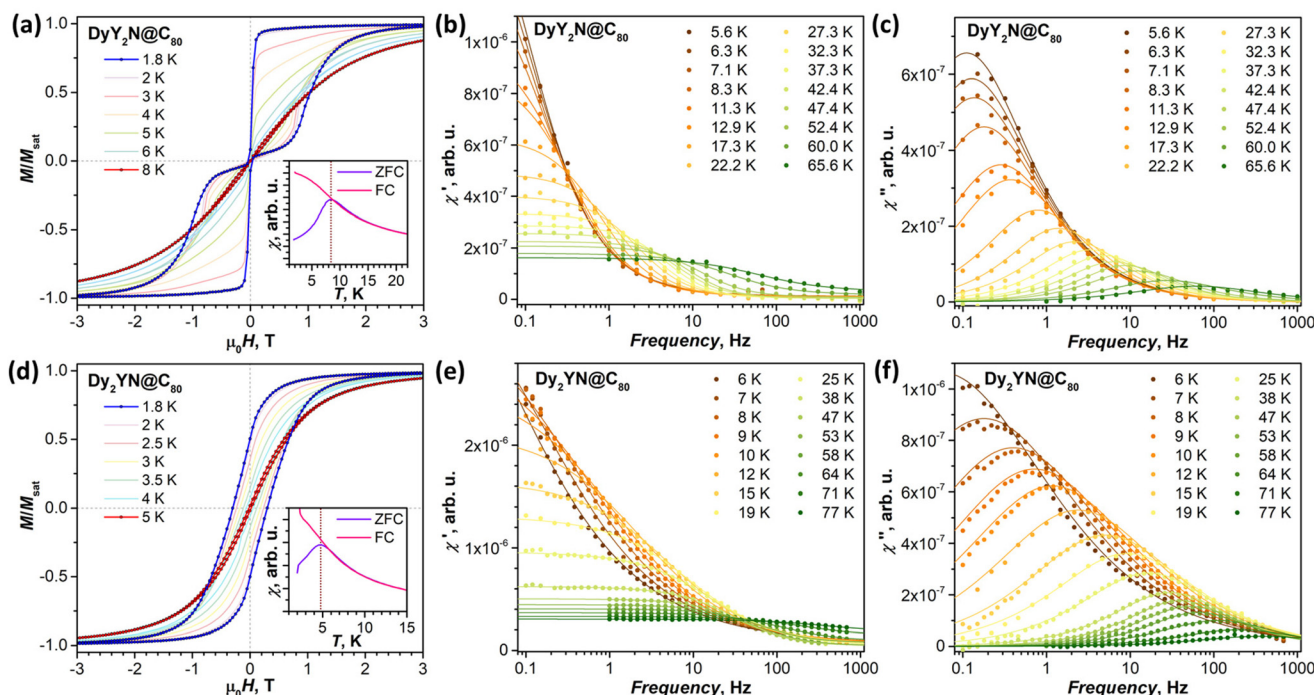
Fig. 6 (a) Magnetic hysteresis of DyY$_2$N@C$_{80}$ (magnetic field sweep rate: 2.9 mT s^{-1}); the inset shows determination of T_B from FC/ZFC measurements (temperature sweep rate: 5 K min^{-1}). (b and c) In-phase χ' (b) and out-of-phase χ'' (c) magnetic susceptibilities of DyY$_2$N@C$_{80}$ measured at different temperatures; dots are experimental values, lines are fitting with the generalized Debye model. (d) Magnetic hysteresis of Dy$_2$YN@C$_{80}$ (magnetic field sweep rate: 2.9 mT s^{-1}); the inset shows determination of T_B from FC/ZFC measurements. (e and f) In-phase χ' (e) and out-of-phase χ'' (f) magnetic susceptibilities of Dy$_2$YN@C$_{80}$ measured at different temperatures; dots are experimental values and lines are fitting with the generalized Debye model.

low temperatures. To determine the sign and size of the Dy···Dy coupling, we employed the effective spin Hamiltonian (eqn (1)) successfully used earlier for other {Dy$_2$} EMFs:[24,99,100,102]

$$\hat{H}_{spin} = \hat{H}_{LF_1} + \hat{H}_{LF_2} - 2j_{12}\hat{J}_1 \cdot \hat{J}_2 + \hat{H}_{ZEE} \quad (1)$$

where $\hat{H}_{LF_1}$ and $\hat{H}_{LF_2}$ are ligand-field Hamiltonians of individual Dy^{3+} ions with parameters from *ab initio* calculations, Dy···Dy coupling is described by the bilinear product of total angular momentum operators of Dy ions ($\hat{J}_1$ and $\hat{J}_2$) scaled by the effective coupling constant j_{12}, and the interaction with the magnetic field is given in the Zeeman term $\hat{H}_{ZEE}$. In essence, the ligand-field terms split the ground-state multiplet of each Dy ion into 8 KDs, whereas the interaction term couples individual KDs of different ions. In the low-energy part of the spectrum, the Hamiltonian gives two quasi-doublets formed by coupling of the ground state KDs of two ions (KD1 and KD1′) with ferromagnetic (FM) and antiferromagnetic (AFM) alignment of magnetic moments (Fig. S7†). The energy difference between the AFM and FM states is:

$$\Delta E_{AFM-FM} = 4J_{z1}J_{z2}j_{12}\cos(\alpha)$$
$$= (g_{z1}/g_J)(g_{z2}/g_J)j_{12}\cos(\alpha) \approx 225j_{12}\cos(\alpha), \quad (2)$$

where J_{z1} and J_{z2} are J_z projections in the ground state KDs of Dy^{3+} ions on individual quantization axes, α is the angle between their quantization axes, g_{z1} and g_{z2} are g_z components

of their pseudospin g-tensors, g_J is the Landé g-factor ($g_J = 4/3$ for the ^{6}H$_{15/2}$ multiplet of Dy^{3+}), and the last approximate term is attributed to $J_{zi} \approx 15/2$. The middle part of the equation emphasizes the similarity of our approach to the method addressing the coupling of Dy moments based on the Lines model[103] and utilizing their ground state pseudospins as popularized by Chibotaru and Ungur *et al.*[104,105] When ligand-field parameters and the angle α are obtained by *ab initio* calculations, j_{12} is the only unknown parameter in eqn (1).

To determine j_{12} and thereby ΔE_{AFM-FM} for Dy$_2$YN@C$_{80}$ and Dy$_2$LaN@C$_{80}$, we measured their magnetization curves at different temperatures between 1.8 and 200 K and fitted them using the Hamiltonian (1) with j_{12} as a free parameter. The *ab initio* ligand-field splitting is already discussed above (Fig. 5 and Tables S4–S6†); the angles between the magnetic moments of 60.6° (Dy$_2$YN) and 63.0° (Dy$_2$LaN) were obtained from the same *ab initio* calculations and are approximately equal to the geometrical angle: $\alpha° \approx 180 - \angle$(Dy–N–Dy). The fits performed employing the PHI code[106] with powder averaging gave the ΔE_{AFM-FM} values of 1.0 ± 0.1 cm^{-1} ($j_{12} = 0.009 \pm 0.001$ cm^{-1}) in Dy$_2$YN@C$_{80}$ and −0.8 ± 0.2 cm^{-1} ($j_{12} = -0.008 \pm 0.002$ cm^{-1}) in Dy$_2$LaN@C$_{80}$ (see Fig. S8 and S9† for comparison of experimental points and fitted curves). These values can be compared to $\Delta E_{AFM-FM} = 5.6$ cm^{-1} in Dy$_2$ScN@C$_{80}$ and $\Delta E_{AFM-FM} = 3.0$ cm^{-1} in Dy$_2$LuN@C$_{80}$.[24] Thus, we conclude that the ΔE_{AFM-FM} value in the Dy$_2$MN@C$_{80}$ series systematically decreases and even changes its sign with the increase of

This journal is © the Partner Organisations 2023

Inorg. Chem. Front., 2023, **10**, 468–484 | **475**

Fig. 7 (a) Magnetic hysteresis measurements for $Dy_2LaN@C_{80}$ (magnetic field sweep rate: 2.9 mT s^{-1}); the inset shows determination of T_B from FC/ZFC measurements. (b) Comparison of the magnetic hysteresis shape for $Dy_2MN@C_{80}$ EMFs (M = Sc, Lu, Y, La) at 2 K (2.1 K for La); magnetic field sweep rate: 2.9 mT s^{-1} for all compounds.

the M^{3+} size. Furthermore, the contribution to ΔE_{AFM-FM} from dipole–dipole interactions can be calculated using geometry parameters and α angles, giving similar values of $\Delta E_{AFM-FM}^{dip} = 3.3–3.4$ cm^{-1} in all $Dy_2MN@C_{80}$ molecules. Therefore, the metal size dependence is mainly caused by the exchange contribution (likely Dy–N–Dy superexchange), which is ferromagnetic in $Dy_2ScN@C_{80}$ ($\Delta E_{AFM-FM}^{exch} = +2.3$ cm^{-1}), but becomes progressively antiferromagnetic in other $Dy_2MN@C_{80}$ molecules with the increase of M (−0.3 cm^{-1} for Lu, −2.4 cm^{-1} for Y, and −4.2 cm^{-1} for La). Interestingly, this systematic variation cannot be well correlated with the cluster geometrical parameters such as the Dy–N bond length (the values are similar for Dy_2LuN and Dy_2LaN), or the Dy–N–Dy angle (the values remain similar for all Dy_2MN), or the degree of cluster pyramidalization (Dy_2ScN and Dy_2LuN are just planar and Dy_2YN is nearly planar). Only the M^{3+} ionic radius appears to be a suitable parameter to correlate with ΔE_{AFM-FM}^{exch} (Fig. 8b).

Relaxation of magnetization

The magnetic hysteresis indicates that the studied EMFs feature single-molecule magnetic behaviour, which calls for a study of the relaxation of magnetization. Relaxation times, τ_M, were measured at different temperatures employing both DC and AC techniques. In the former, the samples were saturated at 7 Tesla, then the field was ramped at 70 mT s^{-1} to 0 T or to 0.2 T, and then a decay of magnetization was measured and fitted with stretched exponential function. This technique allows reliable measurement of τ_M not shorter than 50–100 s; the values longer than 10^4 s are also hard to determine since one would need to measure magnetization decay for a very long time. In AC measurements, the field was oscillated around 0 T with the amplitude of 5 Oe, giving in-phase and out-of-phase magnetic susceptibilities, χ' and χ''. At each temperature, the frequency dependence of χ' and χ'' was measured and the curves were fitted with a generalized Debye model. Fig. 6(b, c, e and f) shows χ' and χ'' data for $DyY_2N@C_{80}$ and $Dy_2YN@C_{80}$. The values of relaxation times are listed in Tables S7 and S8 in the ESI.† The amount of synthesized

Fig. 8 (a) Correlation between reciprocal mass $1/m_M$ and blocking temperature T_B in the $DyM_2N@C_{80}$ series (M = Sc, Y, Lu). (b) Correlation between the ionic radius $R(M^{3+})$ and T_B (left scale, cyan hexagons) and ΔE_{AFM-FM}^{exch} (right scale, red dots) in the $Dy_2MN@C_{80}$ series (M = Sc, Y, Lu, La).

476 | *Inorg. Chem. Front.*, 2023, **10**, 468–484

This journal is © the Partner Organisations 2023

$Dy_2LaN@C_{80}$ was not sufficient for its studies by AC magnetometry.

$DyY_2N@C_{80}$. Due to the QTM, zero-field relaxation times in $DyY_2N@C_{80}$ are comparably short and can be measured only with the AC technique. But the low-temperature τ_M values of 1–2 seconds are close to the frequency limits of the magnetometer, and thus the lowest accessible temperature was 5 K. The τ_M values show a weak temperature dependence at 5–10 K, but then accelerate with the temperature increase. The $\tau_M(T)$-dependence does not exhibit a linear Arrhenius behaviour, at least up to 60 K, at which temperature an onset of a new relaxation regime could be detected. The signal intensity at this temperature is already rather low, thus limiting the available range to $T < 70$ K. The whole dependence could be fitted by a combination of three mechanisms (solid blue line in Fig. 9):

$$\tau_M^{-1}(T) = \tau_{QTM}^{-1} + CT^n + \tau_0^{-1} \exp(-U^{eff}/T) \qquad (3)$$

The QTM regime with $\tau_{QTM} = 2.2 \pm 0.1$ s dominates below 7 K, the Raman regime with $C = (3.1 \pm 0.3) \times 10^{-3}$ s^{-1} K^{-n} and $n = 2.53 \pm 0.03$ has the main contribution up to 55 K, and the Orbach mechanism with an attempt time of $\tau_0 = (2.5 \pm 1.8) \times 10^{-9}$ s^{-1} and an effective barrier of $U^{eff} = 929 \pm 47$ K outweighs the Raman process above 60 K. The Orbach mechanism involving excited ligand-field states is naturally expected for $DyY_2N@C_{80}$, and most probably it is its onset that we detect above 60 K. But since this process can only be attested by a few highest-temperature τ_M points measured at the accuracy limits of our magnetometer, the reliability of the U^{eff} value does not seem sufficient for a discussion of particular KDs involved.

In the finite field of 0.2 T, applied to suppress the QTM, the relaxation times of $DyY_2N@C_{80}$ increased dramatically and

Fig. 9 Magnetization relaxation times of $DyY_2N@C_{80}$ and $Dy_2YN@C_{80}$ determined by DC and AC magnetometry (open points, at 0.2 T; filled points, at zero field). Lines are fits with relaxation mechanisms discussed in the text. The inset shows enlargement of the high-temperature part.

could be measured by the DC technique between 2.8 and 7 K. The values showed a steady decrease with temperature and could be well described by the Raman process with $C = (1.2 \pm 0.1) \times 10^{-6}$ s^{-1} K^{-n} and $n = 5.05 \pm 0.08$ (dashed blue line in Fig. 9). An alternative fit with the Orbach mechanism gave $\tau_0 = 3.0 \pm 0.5$ s^{-1} and $U^{eff} = 21.3 \pm 0.6$ K, similar to the values reported by Wang et al.,[30] but the agreement with the experimental data is worse than that for the Raman mechanism. Note that the removal of the QTM part from eqn (2) and keeping the fitted zero-field parameters for Raman and Orbach mechanisms cannot produce the long relaxation times measured at 0.2 T, indicating that there may be more processes involved in the relaxation and that the mechanism identified at zero field as Raman should be also coupled to the QTM, despite its obvious temperature dependence. Whether the QTM shows unconventional temperature dependence,[72,107] or there may be another relaxation process, which evades detection by AC measurements due to its lower rate, is hard to determine at this moment.

$Dy_2YN@C_{80}$. For $Dy_2YN@C_{80}$, DC (below 4 K) and AC measurements (6–77 K) gave a consistent set of data, which could be described by a combination of the Raman process and two distinct Orbach regimes (cyan line in Fig. 9):

$$\tau_M^{-1}(T) = CT^n + \tau_{0,1}^{-1} \exp(-U_1^{eff}/T) + \tau_{0,2}^{-1} \exp(-U_2^{eff}/T) \qquad (4)$$

The Raman mechanism with $C = (1.11 \pm 0.07) \times 10^{-4}$ s^{-1} K^{-n} and $n = 3.34 \pm 0.06$ describes the low-T part (1.8–4 K) measured by DC magnetometry. The first Orbach regime with $\tau_{0,1} = (1.84 \pm 0.06) \times 10^{-3}$ s^{-1} and a barrier of $U_1^{eff} = 43.8 \pm 0.3$ K is well established between 6 and 50 K, whereas the second Orbach regime with $\tau_{0,2} = (8 \pm 4) \times 10^{-8}$ s^{-1} and a barrier of $U_2^{eff} = 680 \pm 40$ K dominates above 60 K. Similar to the measurements for $DyY_2N@C_{80}$, the parameters of the high-T regime are determined with limited accuracy because of the low signal intensity at these temperatures near the sensitivity limits. Thus, we can hypothesize that this process corresponds to the relaxation *via* ligand-field excited states, but the precise determination of the involved states is hardly possible.

The Orbach regime with a barrier of 44 K (30 cm^{-1}) is quite remarkable. It cannot be assigned to ligand-field excited states since the latter have energies at least an order of magnitude higher (Fig. 5). Thus, U_1^{eff} most likely corresponds to a vibrational mode with a strong spin–phonon coupling. The Arrhenius behavior with the energy equal vibrational frequency was predicted for spin–lattice relaxation coupled to local or optical phonons already back in 1960s[108,109] and re-introduced in more recent theoretical studies.[110] The fullerene cages are rather rigid, and their vibrations occur above 200 cm^{-1}, but the endohedral clusters are composed of heavy atoms and have several modes at low frequencies.[24,62,101] In $Dy_2YN@C_{80}$, the lowest-frequency modes predicted by DFT in harmonic approximation for an isolated molecule are rotational motions (librations) of the cluster at 40.6, 41.1, and 48.3 cm^{-1}. A simple harmonic approximation is most probably not fully suitable for these modes; besides, such intramolecular vibrations can

This journal is © the Partner Organisations 2023

Inorg. Chem. Front., 2023, **10**, 468–484 | **477**

strongly mix with lattice modes,[24] which altogether would affect their frequencies and facilitate the momentum transfer.

In the low-temperature range, the Raman process with a small exponent is only weakly affected by a magnetic field of 0.2 T, presumably *via* the direct mechanism. Note that the relaxation times of $Dy_2YN@C_{80}$ at low temperatures are much longer than those in $DyY_2N@C_{80}$ in zero field, but considerably shorter than the latter in a field of 0.2 T. Thus, the coupling of Dy moments quenches the zero-field QTM, but adds new relaxation pathways, which makes the relaxation of $Dy_2YN@C_{80}$ faster once the QTM in $DyY_2N@C_{80}$ is suppressed. The difference in relaxation times between mono- and dinuclear systems is considerable at higher temperatures as well and remains detectable even when the relaxation starts to be dominated by ligand-field excited states.

Fig. 10 compares magnetization relaxation times in $DyM_2N@C_{80}$ and $Dy_2MN@C_{80}$ series. At low temperatures, all three mono-Dy EMFs show similar relaxation behaviour, including the very long relaxation in a field of 0.2 T and the fast temperature-independent QTM in zero field. The longest time both in zero field and in a finite field is found for
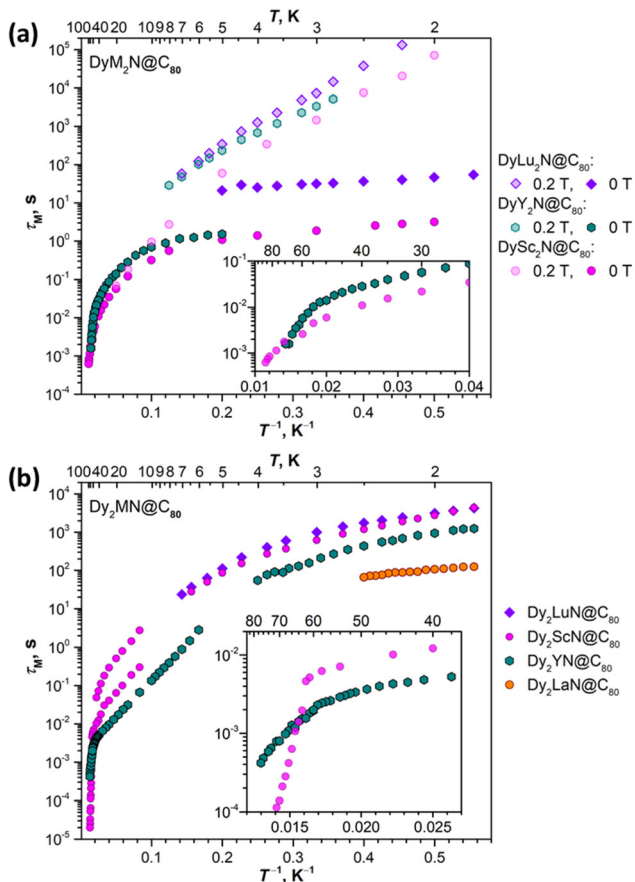

Fig. 10 Magnetization relaxation times of the $DyM_2N@C_{80}$ series (a; M = Sc, Lu, Y; field 0 T and 0.2 T) and $Dy_2MN@C_{80}$ series (b; M = Sc, Lu, Y, La; field 0 T). Insets show enlargement of high-temperature parts. The data for M = Sc are from ref. 72 ($DySc_2N$) and ref. 71 (Dy_2ScN), for M = Lu − from ref. 24.

$DyLu_2N@C_{80}$, followed by $DyY_2N@C_{80}$, and then $DySc_2N@C_{80}$. These data are in line with the row of T_B values for these EMFs. At higher temperatures, $DyY_2N@C_{80}$ and $DySc_2N@C_{80}$ both show a power-law temperature dependence, $DySc_2N@C_{80}$ being again somewhat faster. The data for $DyLu_2N@C_{80}$ in that temperature range are not available as the sample amount in ref. 24 was not sufficient for AC measurements.

The differences in relaxation rates in single-ion magnets can be either attributed to the different single-ion magnetic anisotropy or to the aforementioned spin–phonon interactions. As our computational study showed that the ground-state KD properties of Dy^{3+} are virtually identical (Fig. 5), it makes the differences in the spin–phonon coupling a primary factor. The correlation with the mass of M rather than its size is also a strong indication toward the phonon-based difference in relaxation rates in the $DyM_2N@C_{80}$ series. But the found sequence of relaxation rates ($DySc_2N$ is faster than DyY_2N, and the latter is faster than $DyLu_2N$) is rather counter-intuitive. One could expect a reversed order of relaxation rates because heavier clusters have larger vibrational DOS at lower energies, which facilitates the spin–lattice relaxation at low temperature.

In the $Dy_2MN@C_{80}$ series, the rates determined at low temperature for Dy_2ScN and Dy_2LuN are very similar, while Dy_2YN and Dy_2LaN show progressively faster relaxation. The fast decrease of τ_M falls in line with the decrease of the ΔE_{AFM-FM} difference in this row and hence correlates with the size of M^{3+}. At higher temperatures, the relaxation in $Dy_2YN@C_{80}$ remains faster than that in $Dy_2ScN@C_{80}$ until the switch to the Orbach regime *via* single-ion LF-excitations. At that moment, $Dy_2ScN@C_{80}$ starts to show a faster relaxation as it also has a higher barrier and thus its relaxation accelerates faster with temperature. We conclude that while the relaxation of magnetization in $Dy_2MN@C_{80}$ is governed by a Dy···Dy coupled state, the ΔE_{AFM-FM} value seems to be the main factor in play, and variations of the phonon DOS caused by a different mass of the M ion are less critical.

Photoluminescence of $DyY_2N@C_{80}$

Our earlier finding of thermally activated delayed fluorescence (TADF) in the series of $Y_xSc_{3-x}N@C_{80}$ EMFs $(x = 0–3)$[111,112] suggested that similar phenomena may be present in other $M_3N@C_{80}$ molecules. Indeed, TADF was recently reported in $DyY_2N@C_{80}$.[30] This result was very intriguing since the presence of Dy in the endohedral cluster was expected to increase the spin–orbit coupling and quench the fullerene-based radiative process. As ref. 30 lacked the characterization of the triplet state of $DyY_2N@C_{80}$ below 80 K, we decided to study the photoluminescence (PL) of $DyY_2N@C_{80}$ at helium temperatures. The measurements appeared complicated by a PL signal of the $Y_3N@C_{80}$ trace (which is also identifiable in ref. 30), and additional HPLC cycles were performed to minimize its contribution. After more thorough removal of $Y_3N@C_{80}$ (note that its content was already below the sensitivity of HPLC and MALDI-TOF and could only be assessed by PL measurements), we realized that the spectral features and PL lifetimes of purified $DyY_2N@C_{80}$ are virtually identical to those of $Y_2ScN@C_{80}$

(Fig. S10†).[111] This surprising finding was then confirmed by LDI-TOF mass-spectrometry analysis, which revealed a small signal of $Y_2ScN@C_{80}$ when the measurements were performed with strongly increased laser power; under our standard LDI-TOF measurement conditions, this signal was not detectable (Fig. S11†). Based on these studies, we conclude that $DyY_2N@C_{80}$ is non-luminescent, whereas the PL signals that we and others[30] detected in $DyY_2N@C_{80}$ samples were caused by tiny traces of $Y_3N@C_{80}$ and $Y_2ScN@C_{80}$, which could not be detected by other techniques, but were still measurable in PL spectra. The contamination with $Y_2ScN@C_{80}$ is presumably caused by traces of Sc in the Y_2O_3 oxide used as the Y source in the arc-discharge synthesis. Analogous measurements for $Dy_2YN@C_{80}$ also did not show PL activity.

Conclusions

In this work, we reported the synthesis, isolation, and single-crystal X-ray diffraction study of $Dy_2LaN@I_h\text{-}C_{80}$ and complete $Dy_xY_{3-x}N@I_h\text{-}C_{80}$ series (x = 0–3). The M_3N cluster is found to be planar in all $Dy_xY_{3-x}N$ EMFs, albeit with a systematic increase of the nitrogen out-of-plane amplitude from Y_3N to Dy_3N. The Dy_2LaN cluster is strongly pyramidal with a nitrogen out-of-plane displacement of 0.619(4)/0.530(9) Å. The studies of the magnetic properties of $DyY_2N@C_{80}$, $Dy_2YN@C_{80}$, and $Dy_2LaN@C_{80}$ revealed SMM behavior with magnetic hysteresis in all EMFs but with strongly metal-dependent parameters. Comparison of the relaxation behavior to other $DyM_2N@C_{80}$ and $Dy_2MN@C_{80}$ EMFs (M = Sc, Lu) and extended *ab initio* calculations revealed that the SMM properties in the $DyM_2N@C_{80}$ series can be correlated with the mass of M, whereas the variation of magnetic properties in the $Dy_2MN@C_{80}$ row correlates with the ionic radius of M^{3+}. The mass dependence of spin–lattice relaxation points to a clear connection with the phonon degrees of freedom, whereas the size dependence appears to be related to the variation of the Dy⋯Dy coupling. In particular, the energy of the exchange Dy⋯Dy interaction changes from a positive (ferromagnetic) value of +2.3 cm^{-1} in $Dy_2ScN@C_{80}$ to an antiferromagnetic coupling of −4.2 cm^{-1} in $Dy_2LaN@C_{80}$ with intermediate values of −0.3 cm^{-1} in $Dy_2LuN@C_{80}$ and −2.4 cm^{-1} in $Dy_2YN@C_{80}$. These magneto-structural correlations demonstrate that the variation of the endohedral cluster size and engineering of the inner strain in EMFs can be used as control parameters for tuning the static and dynamic magnetic properties.

Conflicts of interest

There are no conflicts to declare.

Acknowledgements

References

1 L. Dunsch and S. Yang, Metal Nitride Cluster Fullerenes: Their Current State and Future Prospects, *Small*, 2007, **3**(8), 1298–1320.

2 J. Zhang, S. Stevenson and H. C. Dorn, Trimetallic Nitride Template Endohedral Metallofullerenes: Discovery, Structural Characterization, Reactivity, and Applications, *Acc. Chem. Res.*, 2013, **46**(7), 1548–1557.

3 M. N. Chaur, F. Melin, A. L. Ortiz and L. Echegoyen, Chemical, Electrochemical, and Structural Properties of Endohedral Metallofullerenes, *Angew. Chem., Int. Ed.*, 2009, **48**, 7514–7538.

4 A. A. Popov, S. Yang and L. Dunsch, Endohedral Fullerenes, *Chem. Rev.*, 2013, **113**(8), 5989–6113.

5 X. Lu, W. Shen and S. Hu, Endohedral Metallofullerenes: New Structures and Unseen Phenomena, *Chem. – Eur. J.*, 2020, **26**(26), 5748–5757.

6 S. Yang, T. Wei and F. Jin, When metal clusters meet carbon cages: endohedral clusterfullerenes, *Chem. Soc. Rev.*, 2017, **46**(16), 5005–5058.

7 S. Yang, A. A. Popov and L. Dunsch, Carbon Pyramidalization in Fullerene Cages Induced by the Endohedral Cluster: Non-Scandium Mixed Metal Nitride Clusterfullerenes, *Angew. Chem., Int. Ed.*, 2008, **47**, 8196–8200.

8 S. F. Yang, M. Kalbac, A. Popov and L. Dunsch, Gadolinium-based mixed metal nitride clusterfullerenes $Gd_xSc_{3-x}N@C_{80}$ (x = 1, 2), *ChemPhysChem*, 2006, **7**(9), 1990–1995.

9 A. L. Svitova, A. A. Popov and L. Dunsch, Gd/Sc-based Mixed Metal Nitride Cluster Fullerenes: The Mutual Influence of the Cage and Cluster Size and the Role of Sc in the Electronic Structure, *Inorg. Chem.*, 2013, **52**(6), 3368–3380.

10 S. Yang, A. A. Popov, C. Chen and L. Dunsch, Mixed Metal Nitride Clusterfullerenes in Cage Isomers: $Lu_xSc_{3-x}N@C_{80}$ (x = 1, 2) As Compared with $M_xSc_{3-x}N@C_{80}$ (M = Er, Dy, Gd, Nd), *J. Phys. Chem. C*, 2009, **113**(18), 7616–7623.

11 T. Wei, F. Liu, S. Wang, X. Zhu, A. A. Popov and S. Yang, An Expanded Family of Dysprosium–Scandium Mixed-Metal Nitride Clusterfullerenes: The Role of Lanthanide

This journal is © the Partner Organisations 2023

Inorg. Chem. Front., 2023, **10**, 468–484 | **479**

Metal on the Carbon Cage Size Distribution, *Chem. – Eur. J.*, 2015, **21**(15), 5750–5759.

12 Z. Zhang, Y. Liu, P. Han, S. Zhuang, T. Wang, S. Luo and B. Xu, Metallofullerenes Encaging Mixed-Metal Clusters: Synthesis and Structural Studies of $Gd_xHo_{3-x}N@C_{80}$ and $Gd_xLu_{3-x}N@C_{80}$, *ChemPhysChem*, 2015, **16**, 295–298.

13 C. Schlesier, F. Liu, V. Dubrovin, L. Spree, B. Büchner, S. Avdoshenko and A. A. Popov, Mixed dysprosium-lanthanide nitride clusterfullerenes $DyM_2N@C_{80}$-I_h and $Dy_2MN@C_{80}$-I_h (M = Gd, Er, Tm, and Lu): synthesis, molecular structure, and quantum motion of the endohedral nitrogen atom, *Nanoscale*, 2019, **11**, 13139–13153.

14 Y. Zhang, A. A. Popov and L. Dunsch, Endohedral Metal or a Fullerene Cage Based Oxidation? Redox Duality of Nitride Clusterfullerenes $Ce_xM_{3-x}N@C_{78-88}$ (x = 1, 2; M = Sc and Y) Dictated by the Encaged Metals and the Carbon Cage Size, *Nanoscale*, 2014, **6**, 1038–1048.

15 Y. Zhang, S. Schiemenz, A. A. Popov and L. Dunsch, Strain-Driven Endohedral Redox Couple Ce^{IV}/Ce^{III} in Nitride Clusterfullerenes $CeM_2N@C_{80}$ (M = Sc, Y, Lu), *J. Phys. Chem. Lett.*, 2013, **4**, 2404–2409.

16 C. Chen, F. Liu, S. Li, N. Wang, A. A. Popov, M. Jiao, T. Wei, Q. Li, L. Dunsch and S. Yang, Titanium/Yttrium Mixed Metal Nitride Clusterfullerene $TiY_2N@C_{80}$: Synthesis, Isolation, and Effect of the Group-III Metal, *Inorg. Chem.*, 2012, **51**(5), 3039–3045.

17 S. Yang, C. Chen, A. Popov, W. Zhang, F. Liu and L. Dunsch, An endohedral titanium(III) in a clusterfullerene: putting a non-group-III metal nitride into the C_{80}-I_h fullerene cage, *Chem. Commun.*, 2009, 6391–6393.

18 T. Wei, S. Wang, X. Lu, Y. Tan, J. Huang, F. Liu, Q. Li, S. Xie and S. Yang, Entrapping a Group-VB Transition Metal, Vanadium, within an Endohedral Metallofullerene: $V_xSc_{3-x}N@I_h$-C_{80} (x = 1, 2), *J. Am. Chem. Soc.*, 2016, **138**(1), 207–214.

19 M. Nie, J. Xiong, C. Zhao, H. Meng, K. Zhang, Y. Han, J. Li, B. Wang, L. Feng, C. Wang and T. Wang, Luminescent single-molecule magnet of metallofullerene $DyErScN@I_h$-C_{80}, *Nano Res.*, 2019, **12**(7), 1727–1731.

20 M. M. Olmstead, A. de Bettencourt-Dias, J. C. Duchamp, S. Stevenson, H. C. Dorn and A. L. Balch, Isolation and crystallographic characterization of $ErSc_2N@C_{80}$: an endohedral fullerene which crystallizes with remarkable internal order, *J. Am. Chem. Soc.*, 2000, **122**(49), 12220–12226.

21 L. Spree and A. A. Popov, Recent advances in single molecule magnetism of dysprosium-metallofullerenes, *Dalton Trans.*, 2019, **48**(9), 2861–2871.

22 R. Westerström, J. Dreiser, C. Piamonteze, M. Muntwiler, S. Weyeneth, K. Krämer, S.-X. Liu, S. Decurtins, A. Popov, S. Yang, L. Dunsch and T. Greber, Tunneling, remanence, and frustration in dysprosium-based endohedral single-molecule magnets, *Phys. Rev. B: Condens. Matter Mater. Phys.*, 2014, **89**(6), 060406.

23 A. Kostanyan, C. Schlesier, R. Westerström, J. Dreiser, F. Fritz, B. Büchner, A. A. Popov, C. Piamonteze and T. Greber, Gadolinium as an accelerator for reaching thermal equilibrium and its influence on the ground state of $Dy_2GdN@C_{80}$ single-molecule magnets, *Phys. Rev. B*, 2021, **103**(1), 014404.

24 L. Spree, C. Schlesier, A. Kostanyan, R. Westerström, T. Greber, B. Büchner, S. Avdoshenko and A. A. Popov, Single molecule magnets $DyM_2N@C_{80}$ and $Dy_2MN@C_{80}$ (M = Sc, Lu): The impact of diamagnetic metals on the Dy^{3+} magnetic anisotropy, Dy⋯Dy coupling, and mixing of molecular and lattice vibrations, *Chem. – Eur. J.*, 2020, **26**(11), 2436–2449.

25 A. Kostanyan, R. Westerström, D. Kunhardt, B. Büchner, A. A. Popov and T. Greber, Sub-Kelvin hysteresis of the dilanthanide single-molecule magnet $Tb_2ScN@C_{80}$, *Phys. Rev. B*, 2020, **101**(13), 134429.

26 A. Kostanyan, R. Westerström, Y. Zhang, D. Kunhardt, R. Stania, B. Büchner, A. A. Popov and T. Greber, Switching Molecular Conformation with the Torque on a Single Magnetic Moment, *Phys. Rev. Lett.*, 2017, **119**(23), 237202.

27 R. Westerström, J. Dreiser, C. Piamonteze, M. Muntwiler, S. Weyeneth, H. Brune, S. Rusponi, F. Nolting, A. Popov, S. Yang, L. Dunsch and T. Greber, An Endohedral Single-Molecule Magnet with Long Relaxation Times: $DySc_2N@C_{80}$, *J. Am. Chem. Soc.*, 2012, **134**(24), 9840–9843.

28 A. L. Svitova, Y. Krupskaya, N. Samoylova, R. Kraus, J. Geck, L. Dunsch and A. A. Popov, Magnetic moments and exchange coupling in nitride clusterfullerenes $Gd_xSc_{3-x}N@C_{80}$ (x = 1–3), *Dalton Trans.*, 2014, **43**, 7387–7390.

29 Y. Zhang, D. Krylov, S. Schiemenz, M. Rosenkranz, R. Westerstrom, J. Dreiser, T. Greber, B. Buchner and A. A. Popov, Cluster-size dependent internal dynamics and magnetic anisotropy of Ho ions in $HoM_2N@C_{80}$ and $Ho_2MN@C_{80}$ families (M = Sc, Lu, Y), *Nanoscale*, 2014, **6**, 11431–11438.

30 M. Nie, J. Liang, C. Zhao, Y. Lu, J. Zhang, W. Li, C. Wang and T. Wang, Single-Molecule Magnet with Thermally Activated Delayed Fluorescence Based on a Metallofullerene Integrated by Dysprosium and Yttrium Ions, *ACS Nano*, 2021, **15**(12), 19080–19088.

31 J. Dreiser, R. Westerström, Y. Zhang, A. A. Popov, L. Dunsch, K. Krämer, S.-X. Liu, S. Decurtins and T. Greber, The Metallofullerene Field-Induced Single-Ion Magnet $HoSc_2N@C_{80}$, *Chem. – Eur. J.*, 2014, **20**(42), 13536–13540.

32 N. Ishikawa, T. Iino and Y. Kaizu, Determination of Ligand-Field Parameters and f-Electronic Structures of Hetero-Dinuclear Phthalocyanine Complexes with a Diamagnetic Yttrium(III) and a Paramagnetic Trivalent Lanthanide Ion, *J. Phys. Chem. A*, 2002, **106**(41), 9543–9550.

33 L. S. Natrajan, A. J. L. Villaraza, A. M. Kenwright and S. Faulkner, Controlled preparation of a heterometallic lanthanide complex containing different lanthanides in symmetrical binding pockets, *Chem. Commun.*, 2009, (40), 6020–6022.

480 | *Inorg. Chem. Front.*, 2023, **10**, 468–484

This journal is © the Partner Organisations 2023

34 D. Aguilà, L. A. Barrios, V. Velasco, O. Roubeau, A. Repollés, P. J. Alonso, J. Sesé, S. J. Teat, F. Luis and G. Aromí, Heterodimetallic [LnLn'] Lanthanide Complexes: Toward a Chemical Design of Two-Qubit Molecular Spin Quantum Gates, *J. Am. Chem. Soc.*, 2014, **136**(40), 14215–14222.

35 C. D. Buch, S. H. Hansen, D. Mitcov, C. M. Tram, G. S. Nichol, E. K. Brechin and S. Piligkos, Design of pure heterodinuclear lanthanoid cryptate complexes, *Chem. Sci.*, 2021, **12**(20), 6983–6991.

36 J. J. Le Roy, J. Cremers, I. A. Thomlinson, M. Slota, W. K. Myers, P. H. Horton, S. J. Coles, H. L. Anderson and L. Bogani, Tailored homo- and hetero- lanthanide porphyrin dimers: a synthetic strategy for integrating multiple spintronic functionalities into a single molecule, *Chem. Sci.*, 2018, **9**(45), 8474–8481.

37 D. Aguilà, O. Roubeau and G. Aromí, Designed polynuclear lanthanide complexes for quantum information processing, *Dalton Trans.*, 2021, **50**(35), 12045–12057.

38 D. Maniaki, D. Garay-Ruiz, L. A. Barrios, D. O. T. A. Martins, D. Aguilà, F. Tuna, D. Reta, O. Roubeau, C. Bo and G. Aromí, Unparalleled selectivity and electronic structure of heterometallic [LnLn'Ln] molecules as 3-qubit quantum gates, *Chem. Sci.*, 2022, **13**(19), 5574–5581.

39 Z. Zhu, X.-L. Li, S. Liu and J. Tang, External stimuli modulate the magnetic relaxation of lanthanide single-molecule magnets, *Inorg. Chem. Front.*, 2020, **7**(18), 3315–3326.

40 M. Feng, Z.-Y. Ruan, Y.-C. Chen and M.-L. Tong, Physical stimulus and chemical modulations of bistable molecular magnetic materials, *Chem. Commun.*, 2020, **56**(89), 13702–13718.

41 Y. Suzuki, K. Takeda and K. Awaga, Enhancement of Jahn-Teller isomerism in $Mn_{12}Ac$ under high quasi-hydrostatic pressure, *Phys. Rev. B: Condens. Matter Mater. Phys.*, 2003, **67**(13), 132402.

42 A. Sieber, R. Bircher, O. Waldmann, G. Carver, G. Chaboussant, H. Mutka and H.-U. Güdel, Effect of Pressure on the Magnetic Anisotropy in the Single-Molecule Magnet Mn_{12}-Acetate: An Inelastic Neutron Scattering Study, *Angew. Chem., Int. Ed.*, 2005, **44**(27), 4239–4242.

43 R. Bircher, G. Chaboussant, C. Dobe, H. U. Güdel, S. T. Ochsenbein, A. Sieber and O. Waldmann, Single-Molecule Magnets Under Pressure, *Adv. Funct. Mater.*, 2006, **16**(2), 209–220.

44 A. Prescimone, C. J. Milios, S. Moggach, J. E. Warren, A. R. Lennie, J. Sanchez-Benitez, K. Kamenev, R. Bircher, M. Murrie, S. Parsons and E. K. Brechin, [Mn_6] under Pressure: A Combined Crystallographic and Magnetic Study, *Angew. Chem., Int. Ed.*, 2008, **47**(15), 2828–2831.

45 A. Prescimone, C. J. Milios, J. Sanchez-Benitez, K. V. Kamenev, C. Loose, J. Kortus, S. Moggach, M. Murrie, J. E. Warren, A. R. Lennie, S. Parsons and E. K. Brechin, High pressure induced spin changes and magneto-structural correlations in hexametallic SMMs, *Dalton Trans.*, 2009, (25), 4858–4867.

46 P. Parois, S. A. Moggach, J. Sanchez-Benitez, K. V. Kamenev, A. R. Lennie, J. E. Warren, E. K. Brechin, S. Parsons and M. Murrie, Pressure-induced Jahn–Teller switching in a Mn_{12} nanomagnet, *Chem. Commun.*, 2010, **46**(11), 1881–1883.

47 A. M. Thiel, E. Damgaard-Møller and J. Overgaard, High-Pressure Crystallography as a Guide in the Design of Single-Molecule Magnets, *Inorg. Chem.*, 2020, **59**(3), 1682–1691.

48 A. Etcheverry-Berríos, S. Parsons, K. V. Kamenev, M. R. Probert, S. A. Moggach, M. Murrie and E. K. Brechin, Putting the Squeeze on Molecule-Based Magnets: Exploiting Pressure to Develop Magneto-Structural Correlations in Paramagnetic Coordination Compounds, *Magnetochemistry*, 2020, **6**(3), 32.

49 W.-B. Chen, Y.-C. Chen, J.-L. Liu, J.-H. Jia, L.-F. Wang, Q.-W. Li and M.-L. Tong, A Piezochromic Dysprosium(III) Single-Molecule Magnet Based on an Aggregation-Induced-Emission-Active Tetraphenylethene Derivative Ligand, *Inorg. Chem.*, 2017, **56**(15), 8730–8734.

50 M. S. Norre, C. Gao, S. Dey, S. K. Gupta, A. Borah, R. Murugavel, G. Rajaraman and J. Overgaard, High-Pressure Crystallographic and Magnetic Studies of Pseudo-D_{5h} Symmetric Dy(III) and Ho(III) Single-Molecule Magnets, *Inorg. Chem.*, 2020, **59**(1), 717–729.

51 F. Pointillart, J. F. Gonzalez, H. Douib, V. Montigaud, C. McMonagle, B. L. Guennic, O. Cador, D. Pinkowicz and M. Probert, Reversible Pressure-Magnetic Modulation in a Tetrathiafulvalene-Based Dyad Piezochromic Dysprosium Single-Molecule Magnet, *ChemRxiv*, 2022. DOI: **10.26434/chemrxiv-2022-sffw1**.

52 M. Briganti and F. Totti, Magnetic anisotropy on demand exploiting high-pressure as remote control: an ab initio proof of concept, *Dalton Trans.*, 2021, **50**(30), 10621–10628.

53 Q. Deng and A. A. Popov, Clusters encapsulated in Endohedral Metallofullerenes: How strained are they?, *J. Am. Chem. Soc.*, 2014, **136**(11), 4257–4264.

54 S. Stevenson, J. P. Phillips, J. E. Reid, M. M. Olmstead, S. P. Rath and A. L. Balch, Pyramidalization of Gd_3N inside a C_{80} cage. The synthesis and structure of $Gd_3N@C_{80}$, *Chem. Commun.*, 2004, (24), 2814–2815.

55 T. M. Zuo, C. M. Beavers, J. C. Duchamp, A. Campbell, H. C. Dorn, M. M. Olmstead and A. L. Balch, Isolation and structural characterization of a family of endohedral fullerenes including the large, chiral cage fullerenes $Tb_3N@C_{88}$ and $Tb_3N@C_{86}$ as well as the I_h and D_{5h} isomers of $Tb_3N@C_{80}$, *J. Am. Chem. Soc.*, 2007, **129**(7), 2035–2043.

56 R. Valencia, A. Rodriguez-Fortea, A. Clotet, C. de Graaf, M. N. Chaur, L. Echegoyen and J. M. Poblet, Electronic Structure and Redox Properties of Metal Nitride Endohedral Fullerenes $M_3N@C_{2n}$ (M=Sc, Y, La, and Gd; 2n = 80, 84, 88, 92, 96), *Chem. – Eur. J.*, 2009, **15**(41), 10997–11009.

57 M. N. Chaur, F. Melin, J. Ashby, A. Kumbhar, A. M. Rao and L. Echegoyen, Lanthanum Nitride Endohedral

This journal is © the Partner Organisations 2023

Inorg. Chem. Front., 2023, **10**, 468–484 | **481**

Fullerenes La$_3$N@C$_{2n}$ (43 < n < 55): Preferential Formation of La$_3$N@C$_{96}$, *Chem. – Eur. J.*, 2008, **14**(27), 8213–8219.

58 M. N. Chaur, F. Melin, B. Elliott, A. Kumbhar, A. J. Athans and L. Echegoyen, New M$_3$N@C$_{2n}$ Endohedral Metallofullerene Families (M=Nd, Pr, Ce; n = 40–53): Expanding the Preferential Templating of the C$_{88}$ Cage and Approaching the C$_{96}$ Cage, *Chem. – Eur. J.*, 2008, **14**(15), 4594–4599.

59 A. A. Popov, M. Krause, S. F. Yang, J. Wong and L. Dunsch, C$_{78}$ cage isomerism defined by trimetallic nitride cluster size: A computational and vibrational spectroscopic study, *J. Phys. Chem. B*, 2007, **111**(13), 3363–3369.

60 A. A. Popov and L. Dunsch, Structure, Stability, and Cluster-Cage Interactions in Nitride Clusterfullerenes M$_3$N@C$_{2n}$ (M = Sc, Y; 2n = 68–98): a Density Functional Theory Study, *J. Am. Chem. Soc.*, 2007, **129**(38), 11835–11849.

61 W. Shen, L. B. Bao, S. Hu, X. Gao, Y. Xie, X. Gao, W. Huang and X. Lu, Isolation and Crystallographic Characterization of Lu$_3$N@C$_{2n}$ (2n = 80–88): Cage Selection by Cluster Size, *Chem. – Eur. J.*, 2018, **24**(62), 16692–16698.

62 S. F. Yang, S. I. Troyanov, A. A. Popov, M. Krause and L. Dunsch, Deviation from the planarity - a large Dy$_3$N cluster encapsulated in an I$_h$-C$_{80}$ cage: An X-ray crystallographic and vibrational spectroscopic study, *J. Am. Chem. Soc.*, 2006, **128**(51), 16733–16739.

63 Y. Hao, Y. Wang, L. Spree and F. Liu, Rotation of fullerene molecules in the crystal lattice of fullerene/porphyrin: C$_{60}$ and Sc$_3$N@C$_{80}$, *Inorg. Chem. Front.*, 2021, **8**, 122–126.

64 F. Liu and L. Spree, Molecular spinning top: visualizing the dynamics of M$_3$N@C$_{80}$ with variable temperature single crystal X-ray diffraction, *Chem. Commun.*, 2019, **55**(86), 13000–13003.

65 N. Chen, E. Y. Zhang, K. Tan, C. R. Wang and X. Lu, Size effect of encaged clusters on the exohedral chemistry of endohedral fullerenes: A case study on the pyrrolidino reaction of Sc$_x$Gd$_{3-x}$N@C$_{80}$ (x = 0–3), *Org. Lett.*, 2007, **9**(10), 2011–2013.

66 S. Aroua, M. Garcia-Borràs, S. Osuna and Y. Yamakoshi, Essential Factors for Control of the Equilibrium in the Reversible Rearrangement of M$_3$N@I$_h$-C$_{80}$ Fulleropyrrolidines: Exohedral Functional Groups versus Endohedral Metal Clusters, *Chem. – Eur. J.*, 2014, **20**(43), 14032–14039.

67 C. M. Cardona, A. Kitaygorodskiy and L. Echegoyen, Trimetallic nitride endohedral metallofullerenes: Reactivity dictated by the encapsulated metal cluster, *J. Am. Chem. Soc.*, 2005, **127**(29), 10448–10453.

68 N. Chen, L. Z. Fan, K. Tan, Y. Q. Wu, C. Y. Shu, X. Lu and C. R. Wang, Comparative Spectroscopic and Reactivity Studies of Sc$_{3-x}$Y$_x$N@C$_{80}$ (x = 0–3), *J. Phys. Chem. C*, 2007, **111**(32), 11823–11828.

69 K. Junghans, K. B. Ghiassi, N. A. Samoylova, Q. Deng, M. Rosenkranz, M. M. Olmstead, A. L. Balch and

A. A. Popov, Synthesis and Isolation of the Titanium-Scandium Endohedral Fullerenes – Sc$_2$TiC@I$_h$-C$_{80}$, Sc$_2$TiC@D$_{5h}$-C$_{80}$, and Sc$_2$TiC$_2$@I$_h$-C$_{80}$: Metal Size Tuning of the Ti^{IV}/Ti^{III} Redox Potentials, *Chem. – Eur. J.*, 2016, **22**(37), 13098–13107.

70 K. Junghans, C. Schlesier, A. Kostanyan, N. A. Samoylova, Q. Deng, M. Rosenkranz, S. Schiemenz, R. Westerström, T. Greber, B. Büchner and A. A. Popov, Methane as a Selectivity Booster in the Arc-Discharge Synthesis of Endohedral Fullerenes: Selective Synthesis of the Single-Molecule Magnet Dy$_2$TiC@C$_{80}$ and Its Congener Dy$_2$TiC$_2$@C$_{80}$, *Angew. Chem., Int. Ed.*, 2015, **54**(45), 13411–13415.

71 D. S. Krylov, F. Liu, S. M. Avdoshenko, L. Spree, B. Weise, A. Waske, A. U. B. Wolter, B. Büchner and A. A. Popov, Record-high thermal barrier of the relaxation of magnetization in the nitride clusterfullerene Dy$_2$ScN@C$_{80}$-I$_h$, *Chem. Commun.*, 2017, **53**, 7901–7904.

72 D. Krylov, F. Liu, A. Brandenburg, L. Spree, V. Bon, S. Kaskel, A. Wolter, B. Buchner, S. Avdoshenko and A. A. Popov, Magnetization relaxation in the single-ion magnet DySc$_2$N@C$_{80}$: quantum tunneling, magnetic dilution, and unconventional temperature dependence, *Phys. Chem. Chem. Phys.*, 2018, **20**, 11656–11672.

73 S. Yang, L. Zhang, W. Zhang and L. Dunsch, A Facile Route to Metal Nitride Clusterfullerenes by Using Guanidinium Salts: A Selective Organic Solid as the Nitrogen Source, *Chem. – Eur. J.*, 2010, **16**(41), 12398–12405.

74 Y. Zhang, K. B. Ghiassi, Q. Deng, N. A. Samoylova, M. M. Olmstead, A. L. Balch and A. A. Popov, Synthesis and Structure of LaSc$_2$N@C$_s$(hept)-C$_{80}$ with One Heptagon and Thirteen Pentagons, *Angew. Chem., Int. Ed.*, 2015, **52**(2), 495–499.

75 S. Stevenson, C. B. Rose, J. S. Maslenikova, J. R. Villarreal, M. A. Mackey, B. Q. Mercado, K. Chen, M. M. Olmstead and A. L. Balch, Selective Synthesis, Isolation, and Crystallographic Characterization of LaSc$_2$N@I$_h$-C$_{80}$, *Inorg. Chem.*, 2012, **51**(24), 13096–13102.

76 L. Dunsch, S. Yang, L. Zhang, A. Svitova, S. Oswald and A. A. Popov, Metal Sulfide in a C$_{82}$ Fullerene Cage: A New Form of Endohedral Clusterfullerenes, *J. Am. Chem. Soc.*, 2010, **132**(15), 5413–5421.

77 U. Mueller, R. Förster, M. Hellmig, F. U. Huschmann, A. Kastner, P. Malecki, S. Pühringer, M. Röwer, K. Sparta, M. Steffien, M. Ühlein, P. Wilk and M. S. Weiss, The macromolecular crystallography beamlines at BESSY II of the Helmholtz-Zentrum Berlin: Current status and perspectives, *Eur. Phys. J. Plus*, 2015, **130**(7), 141.

78 W. Kabsch, XDS, *Acta Crystallogr., Sect. D: Biol. Crystallogr.*, 2010, **66**(2), 125–132.

79 K. M. Sparta, M. Krug, U. Heinemann, U. Mueller and M. S. Weiss, XDSAPP2.0, *J. Appl. Crystallogr.*, 2016, **49**(3), 1085–1092.

80 G. Sheldrick, Crystal structure refinement with SHELXL, *Acta Crystallogr., Sect. C: Struct. Chem.*, 2015, **71**(1), 3–8.

482 | *Inorg. Chem. Front.*, 2023, **10**, 468–484

This journal is © the Partner Organisations 2023

81 M. M. Olmstead, T. Zuo, H. C. Dorn, T. Li and A. L. Balch, Metal ion size and the pyramidalization of trimetallic nitride units inside a fullerene cage: Comparisons of the crystal structures of $M_3N@I_h$-C_{80} (M = Gd, Tb, Dy, Ho, Er, Tm, Lu, and Sc) and some mixed metal counterparts, *Inorg. Chim. Acta*, 2017, **468**, 321–326.

82 T. Zuo, M. M. Olmstead, C. M. Beavers, A. L. Balch, G. Wang, G. T. Yee, C. Shu, L. Xu, B. Elliott, L. Echegoyen, J. C. Duchamp and H. C. Dorn, Preparation and Structural Characterization of the I_h and the D_{5h} Isomers of the Endohedral Fullerenes $Tm_3N@C_{80}$: Icosahedral C_{80} Cage Encapsulation of a Trimetallic Nitride Magnetic Cluster with Three Uncoupled Tm^{3+} Ions, *Inorg. Chem.*, 2008, **47**(12), 5234–5244.

83 L. Echegoyen, C. J. Chancellor, C. M. Cardona, B. Elliott, J. Rivera, M. M. Olmstead and A. L. Balch, X-Ray crystallographic and EPR spectroscopic characterization of a pyrrolidine adduct of $Y_3N@C_{80}$, *Chem. Commun.*, 2006, (25), 2653–2655.

84 C. Shu, W. Xu, C. Slebodnick, H. Champion, W. Fu, J. E. Reid, H. Azurmendi, C. Wang, K. Harich, H. C. Dorn and H. W. Gibson, Syntheses and Structures of Phenyl-C_{81}-Butyric Acid Methyl Esters (PCBMs) from $M_3N@C_{80}$, *Org. Lett.*, 2009, **11**(8), 1753–1756.

85 S. Stevenson, H. R. Thompson, K. D. Arvola, K. B. Ghiassi, M. M. Olmstead and A. L. Balch, Isolation of $CeLu_2N@I_h$-C_{80} through a Non-Chromatographic, Two-Step Chemical Process and Crystallographic Characterization of the Pyramidalized $CeLu_2N$ within the Icosahedral Cage, *Chem. – Eur. J.*, 2015, **21**(29), 10362–10368.

86 S. Stevenson, C. Chancellor, H. M. Lee, M. M. Olmstead and A. L. Balch, Internal and External Factors in the Structural Organization in Cocrystals of the Mixed-Metal Endohedrals ($GdSc_2N@I_h$-C_{80}, $Gd_2ScN@I_h$-C_{80}, and $TbSc_2N@I_h$-C_{80}) and Nickel(II) Octaethylporphyrin, *Inorg. Chem.*, 2008, **47**(5), 1420–1427.

87 V. Dubrovin, L.-H. Gan, B. Büchner, A. A. Popov and S. M. Avdoshenko, Endohedral metal-nitride cluster ordering in metallofullerene–Ni^{II}(OEP) complexes and crystals: a theoretical study, *Phys. Chem. Chem. Phys.*, 2019, **21**, 8197–8200.

88 Y. Wang, G. Velkos, N. J. Israel, M. Rosenkranz, B. Büchner, F. Liu and A. A. Popov, Electrophilic Trifluoromethylation of Dimetallofullerene Anions en Route to Air-Stable Single-Molecule Magnets with High Blocking Temperature of Magnetization, *J. Am. Chem. Soc.*, 2021, **143**(43), 18139–18149.

89 A. A. Popov and L. Dunsch, The Bonding Situation in Endohedral Metallofullerenes as Studied by Quantum Theory of Atoms in Molecules (QTAIM), *Chem. – Eur. J.*, 2009, **15**(38), 9707–9729.

90 L. Ungur and L. F. Chibotaru, Ab Initio Crystal Field for Lanthanides, *Chem. – Eur. J.*, 2017, **23**(15), 3708–3718.

91 R. Shannon, Revised effective ionic radii and systematic studies of interatomic distances in halides and chalcogenides, *Acta Crystallogr., Sect. A: Cryst. Phys., Diffr., Theor. Gen. Crystallogr.*, 1976, **32**(5), 751–767.

92 F. Aquilante, J. Autschbach, A. Baiardi, S. Battaglia, V. A. Borin, L. F. Chibotaru, I. Conti, L. D. Vico, M. Delcey, I. F. Galván, N. Ferré, L. Freitag, M. Garavelli, X. Gong, S. Knecht, E. D. Larsson, R. Lindh, M. Lundberg, P. Å Malmqvist, A. Nenov, J. Norell, M. Odelius, M. Olivucci, T. B. Pedersen, L. Pedraza-González, Q. M. Phung, K. Pierloot, M. Reiher, I. Schapiro, J. Segarra-Martí, F. Segatta, L. Seijo, S. Sen, D.-C. Sergentu, C. J. Stein, L. Ungur, M. Vacher, A. Valentini and V. Veryazov, Modern quantum chemistry with [Open]Molcas, *J. Chem. Phys.*, 2020, **152**(21), 214117.

93 L. F. Chibotaru and L. Ungur, Ab initio calculation of anisotropic magnetic properties of complexes. I. Unique definition of pseudospin Hamiltonians and their derivation, *J. Chem. Phys.*, 2012, **137**(6), 064112.

94 J. Dreiser, Molecular lanthanide single-ion magnets: from bulk to submonolayers, *J. Phys.: Condens. Matter*, 2015, **27**(18), 183203.

95 T. G. Ashebr, H. Li, X. Ying, X.-L. Li, C. Zhao, S. Liu and J. Tang, Emerging Trends on Designing High-Performance Dysprosium(III) Single-Molecule Magnets, *ACS Mater. Lett.*, 2022, **4**, 307–319.

96 W. Cai, J. D. Bocarsly, A. Gomez, R. J. Letona Lee, A. Metta-Magaña, R. Seshadri and L. Echegoyen, High blocking temperatures for DyScS endohedral fullerene single-molecule magnets, *Chem. Sci.*, 2020, **11**, 13129–13136.

97 C. Schlesier, L. Spree, A. Kostanyan, R. Westerström, A. Brandenburg, A. U. B. Wolter, S. Yang, T. Greber and A. A. Popov, Strong carbon cage influence on the single molecule magnetism in Dy–Sc nitride clusterfullerenes, *Chem. Commun.*, 2018, **54**(70), 9730–9733.

98 A. Brandenburg, D. S. Krylov, A. Beger, A. U. B. Wolter, B. Büchner and A. A. Popov, Carbide clusterfullerene $DyYTiC@C_{80}$ featuring three different metals in the endohedral cluster and its single-ion magnetism, *Chem. Commun.*, 2018, **54**(76), 10683–10686.

99 G. Velkos, W. Yang, Y.-R. Yao, S. M. Sudarkova, F. Liu, S. Avdoshenko, N. Chen and A. A. Popov, Metallofullerene single-molecule magnet $Dy_2O@C_{2v}(5)$-C_{80} with a strong antiferromagnetic Dy···Dy coupling, *Chem. Commun.*, 2022, **58**, 7164–7167.

100 W. Yang, G. Velkos, F. Liu, S. M. Sudarkova, Y. Wang, J. Zhuang, H. Zhang, X. Li, X. Zhang, B. Büchner, S. M. Avdoshenko, A. A. Popov and N. Chen, Single Molecule Magnetism with Strong Magnetic Anisotropy and Enhanced Dy···Dy Coupling in Three Isomers of Dy-Oxide Clusterfullerene $Dy_2O@C_{82}$, *Adv. Sci.*, 2019, **6**(20), 1901352.

101 C.-H. Chen, D. S. Krylov, S. M. Avdoshenko, F. Liu, L. Spree, R. Yadav, A. Alvertis, L. Hozoi, K. Nenkov, A. Kostanyan, T. Greber, A. U. B. Wolter and A. A. Popov, Selective arc-discharge synthesis of Dy_2S-clusterfullerenes

This journal is © the Partner Organisations 2023

Inorg. Chem. Front., 2023, **10**, 468–484 | **483**

and their isomer-dependent single molecule magnetism, *Chem. Sci.*, 2017, **8**(9), 6451–6465.

102 D. Krylov, G. Velkos, C.-H. Chen, B. Büchner, A. Kostanyan, T. Greber, S. Avdoshenko and A. A. Popov, Magnetic hysteresis and strong ferromagnetic coupling of sulfur-bridged Dy ions in clusterfullerene $Dy_2S@C_{82}$, *Inorg. Chem. Front.*, 2020, **7**, 3521–3532.

103 M. E. Lines, Orbital Angular Momentum in the Theory of Paramagnetic Clusters, *J. Chem. Phys.*, 1971, **55**(6), 2977–2984.

104 L. Ungur, W. Van den Heuvel and L. F. Chibotaru, Ab initio investigation of the non-collinear magnetic structure and the lowest magnetic excitations in dysprosium triangles, *New J. Chem.*, 2009, **33**(6), 1224–1230.

105 L. F. Chibotaru, L. Ungur and A. Soncini, The Origin of Nonmagnetic Kramers Doublets in the Ground State of Dysprosium Triangles: Evidence for a Toroidal Magnetic Moment, *Angew. Chem., Int. Ed.*, 2008, **47**(22), 4126–4129.

106 N. F. Chilton, R. P. Anderson, L. D. Turner, A. Soncini and K. S. Murray, PHI: A powerful new program for the analysis of anisotropic monomeric and exchange-coupled polynuclear d- and f-block complexes, *J. Comput. Chem.*, 2013, **34**(13), 1164–1175.

107 Y.-S. Ding, K.-X. Yu, D. Reta, F. Ortu, R. E. P. Winpenny, Y.-Z. Zheng and N. F. Chilton, Field- and temperature-dependent quantum tunnelling of the magnetisation in a large barrier single-molecule magnet, *Nat. Commun.*, 2018, **9**(1), 3134.

108 P. G. Klemens, Localized Modes and Spin-Lattice Interactions, *Phys. Rev.*, 1962, **125**(6), 1795–1798.

109 C.-Y. Huang, Optical Phonons in Electron Spin Relaxation, *Phys. Rev.*, 1967, **154**(2), 215–219.

110 A. Lunghi, F. Totti, R. Sessoli and S. Sanvito, The role of anharmonic phonons in under-barrier spin relaxation of single molecule magnets, *Nat. Commun.*, 2017, **8**, 14620.

111 M. Zalibera, F. Ziegs, S. Schiemenz, V. Dubrovin, W. Lubitz, A. Savitsky, S. Deng, X.-B. Wang, S. Avdoshenko and A. A. Popov, Metallofullerene photoswitches driven by photoinduced fullerene-to-metal electron transfer, *Chem. Sci.*, 2021, **12**, 7818–7838.

112 M. Zalibera, D. S. Krylov, D. Karagiannis, P.-A. Will, F. Ziegs, S. Schiemenz, W. Lubitz, S. Reineke, A. Savitsky and A. A. Popov, Thermally Activated Delayed Fluorescence in a $Y_3N@C_{80}$ Endohedral Fullerene: Time-Resolved Luminescence and EPR Studies, *Angew. Chem., Int. Ed.*, 2018, **57**(1), 277–281.

484 | *Inorg. Chem. Front.*, 2023, **10**, 468–484

This journal is © the Partner Organisations 2023